12-2005

Biomimetic Membranes Realized with Arrays of Carbon Nanofibers

Eric Hullander
University of Tennessee - Knoxville

To the Graduate Council:

I am submitting herewith a thesis written by Eric Hullander entitled "Biomimetic Membranes Realized with Arrays of Carbon Nanofibers." I have examined the final electronic copy of this thesis for form and content and recommend that it be accepted in partial fulfillment of the requirements for the degree of Master of Science, with a major in Electrical Engineering.

Michael L. Simpson, Major Professor

We have read this thesis and recommend its acceptance:

Gregory Peterson, Jayne Wu

Accepted for the Council:
Carolyn R. Hodges

Vice Provost and Dean of the Graduate School

(Original signatures are on file with official student records.)

To the Graduate Council:

I am submitting herewith a thesis written by Eric Hullander entitled "Biomimetic Membranes Realized with Arrays of Carbon Nanofibers". I have examined the final electronic copy of this thesis for form and content and recommend that it be accepted in partial fulfillment of the requirements for the degree of Master of Science, with a major in Electrical Engineering.

Michael L. Simpson
Major Professor

We have read this thesis
and recommend its acceptance:

Gregory Peterson

Jayne Wu

Accepted for the Council:

Anne Mayhew
Vice Chancellor and
Dean of Graduate Studies

(Original signatures are on file with the official student records.)

Biomimetic Membranes

Realized with Arrays of

Carbon Nanofibers

A Thesis

Presented for the

Master of Science

Degree

The University of Tennessee, Knoxville

Eric Hullander

December 2005

Aknowledgements

I thank Dr. Michael Simpson and Dr. Mitchel Doktycz for their patience, wisdom, and the opportunity to work on this project. I thank Dr. Anatoli Melechko for sharing with me his expertise in microfabrication and guidance on countless other topics. I thank Tim McKnight for many valuable suggestions regarding surface chemistry. I thank Dr. Laura Morris Edwards for her valuable critiques of my technical writing. I thank the entire MENT group for all of their support. I thank Dr. Syed Islam and Dr. Michael Roberts for their patience and guidance. I thank my parents for their love. I thank God.

Abstract

A microfluidic device with imbedded nanoporous membranes, constructed using a novel nanostructured material, was designed, built, modeled, and tested. The membranes were shown to be modular, and by adsorbing monodisperse latex spheres to the fibrous membrane, the pore size could be controlled. A mathematical model of the device was developed based on several existing fluidic models for transport through fibrous materials, and an image processing algorithm was designed to extract the hydrodynamic properties of the device from a series of scanning electron micrographs based on the existing hydrodynamic models. A series of experiments were performed using fluorescent microscopy to quantify the hydrodynamic properties of the device. The results of these experiments suggest that the modeling was accurate. This thesis explores several unique issues. The first is that tortuosity, defined as a particle's path length divided by its displacement, is the factor that scales the reference diffusion. The second is that the membrane can be thought of as a realization of random fractal. The third is that tortuosity can be related to the resistance scaling factor, a property of a fractal. To support these claims, a close agreement between a classical and a fractal permeability model is shown. In addition, a model is incorporated to approximate surface effects showing that the surface cannot be categorically neglected because of the rather large device dimensions. Finally, the extrapolation of 3-dimensional information from an SEM image is used to determine the model parameters.

Table of Contents

List of Tables

List of Figures

1 A Small Revolution

1.1 Advantages of Being Small

On December 29th 1959, Richard Feynman gave his classic talk "There's Plenty of Room at the Bottom" at the annual meeting of the American Physical Society at Caltech. This speech forecasted one of the most important revolutions in human history. Some might say that it was a self-fulfilling prophecy, inspiring the revolution that we are in the midst of today. What Feynman was speaking of was the miniaturization and resulting integration of technology. In his words,

> "It is a staggeringly small world that is below. In the year 2000, when they look back at this age, they will wonder why it was not until the year 1960 that anybody began seriously to move in this direction."[1a]

Of course, scientists had been looking in this direction for some time, but it may not have been until the 1960s that people began to realize en masse that miniaturization was a solution to many technological problems.

In the 1930s, Bell Lab's director of research Mervin Kelly recognized that the vacuum tube needed to be replaced by a better device in order for the telephone industry to grow. He suspected that a semiconductor device might work. After years of work, a group of eight scientists and engineers led by Bill Shockley of Bell Labs unveiled the first transistor to the world in 1948. The transistor is smaller, cheaper, more energy efficient, and has a longer useful life than the vacuum tube. The invention received little attention at the time, but is an indispensable device today. So the solution to Bell Lab's vacuum tube problem was the transistor, a smaller device. The members of the eight-

man team went on to form the companies Fairchild Semiconductor and Intel, where the miniaturization paradigm continued.[2a]

Around the same time as Feynman's speech, Jack Kilby of Texas instruments and Robert Noyce of Fairchild Semiconductor independently invented what is now known as the integrated circuit (IC). Until then, complex machines such as computers required larger and larger numbers of discrete components. The monolithic IC placed all of the individual transistors, resistors, capacitors, and connecting wires on a single crystal made of semiconductor material. Kilby, an electrical engineer with a background in ceramic-based silkscreen circuit boards, used germanium for his devices, and Noyce, co-founder of Fairchild Semiconductor, used the more familiar element, silicon. Both parties received patents in 1959 for their work, and after cross licensing, their technologies gave birth to a one trillion-dollar annual global market. The inventors, however, did not have the foresight that Feynman had. According to Kilby,

> "What we didn't realize then was that the integrated circuit would reduce the cost of electronic functions by a factor of a million to one. Nothing had ever done that for anything before."[3a]

The trend of miniaturization and integration was well on its way, at least in the field of electronics, by the time Feynman gave his galvanizing speech. The leaders of this trend most likely did not realize all of the implications of their work.

1.2 Moore's Law

The rate at which Feynman's vision is being implemented is known as Moore's Law in computer science. Gordon Moore, one of the founders of Intel, observed in 1965 that the number of transistors in ICs doubled every year. This observation has been elevated to the status of a law and has set the standard rate of progress for the electronics industry for nearly four decades. In 1965, 30 transistors could be fit into an IC; in 2002, 55 million transistors could be fit into Intel's Pentium 4 IC. The motivation behind increasing the transistor count is to improve performance. As the number of devices on a single chip increases, almost all parameters of performance are improved. Countless devices can be fabricated in a single run, and this drives down the cost. More devices allow sophisticated circuits to be fabricated that can perform difficult tasks in a shorter amount of time. In order to fit all of these devices onto a single chip, the individual transistors on the chip must be made smaller. Also, smaller devices consume less power, and are therefore more energy efficient.[4a] Moore's Law today has been expanded to mean the rate at which technology progresses. It is now the expectation that **technology** should progress exponentially, not simply the number of transistors on an integrated circuit. In order to keep up with the demands of Moore's Law, companies are employing three intertwined strategies. These strategies are to continue increasing the transistor count, to create more complex circuits, and to converge existing technologies together onto one chip.[4a] Intel is currently working on a MOS capacitor waveguide phase shifter allowing monolithic integration of photonic modulators onto a single IC. This would allow information to be encoded onto a beam of light, which has much greater

bandwidth and would thus increase the speed of communication between connected devices, be they inside the PC or PC to PC.[4a] Once again the trend towards miniaturization and integration is paving the way to a brighter future, and there is still plenty of room at the bottom.

The convergence of existing technologies is perhaps one of the most interesting of the strategies being used to implement Moore's Law. This is because peripheral technologies will be forced to shrink and to integrate at the same exponential rate as electronics have been, according to Moore. The idea that technology should grow exponentially is influencing other fields such micro-electro-mechanical systems (MEMS), biotechnology, and microfluidics. At least, this is the current vision at Intel.[4a]

1.3 MEMS

In the 1970s and 1980s, researchers began producing silicon pressure sensors. Researchers began to realize the potential use of silicon for non-electronic devices as was outlined in Kurt Peterson's "Silicon as a Structural Material".[22a] This was the genesis of the MEMS revolution. MEMS are integrated systems combining electrical and mechanical components. MEMS are fabricated using the same processing techniques and equipment as ICs, and, for this reason the field has developed quickly. In addition, since MEMS are fabricated using IC techniques, the same advantages that have made the semiconductor industry a success benefit MEMS. Thousands can be fabricated in a single run, thus greatly reducing cost and space. MEMS are also very small integrated devices with built-in electronic systems, thus making them less cumbersome than other

devices. This integration allows a wide array of highly functional devices to be fabricated in a tight compact package. Some of the types of devices that have been made include miniature sensors, controllers, and actuators. Presently, there are few commercial applications for this family of devices (some MEMS are used as pressure sensors and collision detectors for air-bag deployment), but the possibilities are great. They can be used as fluid pumps and valves, as well as optical scanners or mirror arrays.[14a]

Microfluidic devices could be considered a subset of MEMS. Microfluidics is a field that has flourished in the last quarter century in the hinterland between biotechnology, microtechnology, physics, and analytical chemistry.[5a, 6a] Microfluidics, as the name implies, is the science and engineering of micrometer scale fluidic systems. At this scale, some physical processes such as diffusion,[7a] osmotic movement, electrophoretic motility, and surface interactions, are enhanced [6a] while others such as gravity and inertial forces are diminished.[1a] Microfluidic devices use these processes and integrate them with other technologies to perform tasks that would otherwise be expensive and difficult to do at the macro-scale. In addition, their monolithic nature streamlines their production. Some other advantages that microfluidic devices have over their bench-top counterparts are economy of size, economy of processing time, economy of power consumption, minimization of waste and reagent volume, flexibility of design, disposability, and portability.[6a,8a]

The first microfluidic systems were fabricated in silicon and glass by adapting fabrication techniques developed for the microelectronics industry into micromachining techniques. Today, polymers are also being used because they are simpler and cheaper to

process. Of these polymers, SU-8 [10a] and polydimethylsiloxane (PDMS) [8a] are being used extensively.[6a,8a]

These devices have found many applications such as performing chemical reactions, biochemical analysis of proteins and peptides, DNA typing via PCR amplification, and in cell-based assays.[8a, 6a] Microfluidic devices allow for highly sensitive assaying, which is particularly important for scarce protein samples.[6a] As microfabrication and micromachining techniques improve, the scale of microelectronics, MEMS and microfluidic devices will also keep shrinking, and new technologies will be integrated into them. Some of these devices are being referred to as examples of nanotechnology.

1.4 Nanotechnology

Nanotechnology is the burgeoning science of the small. It is a big field, but the actual size of the technology is unimaginably tiny, typically less than one micron. Some only consider objects smaller than 100 nm to be "nano", but these choices of dimensions are, of course, completely arbitrary since a meter is an arbitrary unit of length and 100 nm is just ten millionths of that. However, interesting physical phenomena begin to take place at very small scales, and it is these phenomena that scientists and engineers wish to exploit. Like microfluidics and MEMS, nanotechnology is also a descendant of microelectronics.[9a] The latest CMOS technology has features that have shrunk to less than a micron, and as technology keeps pushing the limits of Moore's Law, it is inevitable that microelectronic features will need to shrink to less than 100 nm.[4a] This means that microelectronics could soon be called *nanoelectronics*. At some point in the

future, however, traditional fabrication techniques will fail to be able to produce ever-smaller devices. Scientists are now hard at work trying to develop new techniques [12a] to maintain an iron grip on the vice of Moore's Law.[12a,4a]

Though its roots are in microelectronics, the scope of nanotechnology is much broader. Nanotechnology has its sticky fingers in several other scientific disciplines such as biology [11a], chemistry [13a], and microfluidics.[5a] It is expected that nanotechnology will be developed at three levels: materials, devices, and systems. Currently, nanomaterials are the most advanced in both scientific knowledge and commercial applications.[11a] Nanomaterials are materials whose constituent particles have at least one dimension that is less than 100 nm. This size range includes but is not limited to atoms and molecules that may or may not occur naturally. Chemistry and biology are well-developed disciplines that analyze and synthesize molecular compounds whose constituent particles are nanoscale, so nanotechnology could be seen as an extension of these disciplines.[9a] Also included under this moniker is a litany of other higher order manmade structures. Many of these structures are named after an object in the macro-world that they resemble with the prefix "nano" (derived from the ancient Greek word for dwarf) attached to the front. This set includes, but is not limited to, nanofibers, nanorods, nanocones, nanopores, nanotubes, nanowires, nanopipes, nanodots, and nanocapillaries.

1.5 Two Approaches

There are two approaches to creating nanostructures, top-down and bottom-up.[14a] Top-down processes tear down everything that is unwanted, while bottom-up

processes build up everything that is wanted. The New York City subways were built using a top-down approach while the skyline was built using a bottom-up approach. Nanomachining, an extension of micromachining, is a top-down approach.[14a] Micromachining and nanomachining rely on masks to create patterns on a substrate. As the feature size shrinks, shorter wavelengths and thinner resists are required for photolithography. The minimum feature size, b_{min}, is given by

$$b_{\min} = \frac{3}{2}(\lambda s)^{\frac{1}{2}}$$

where λ is the wavelength and s is the resist thickness.[15a] In some cases electron beam lithography (EBL) and focused ion beam (FIB) milling are used. These processes, unfortunately, have low throughput and are expensive.[16a] Soft lithography,[8a] nanoimprint lithography,[16a] and self-assembling lithography[12a,14a] promise to help ameliorate these problems, but may not be compatible with existing microfabrication techniques.

Nanochemistry, an extension of chemistry and biology [9a], is a bottom-up approach.[14a] Nanochemistry relies on biological or biomimetic processes to form nanoscale structures. Biological systems are famous for their ability to cheaply create scads of complex nanoscale structures by self-assembly. This is the technique that scientists strive to mimic.[14a, 12a] Examples of these processes in nature include transcription and translation of nucleic and amino acids, crystal growth [14a], and silicatein formation.[17a] A disadvantage of self-assembly is that it is difficult to create

non-periodic structures.[12a] Mechanosynthesis [14a] is a hypothetical bottom-up process, but its validity has not been verified.[18a]

1.6 Nanobiotechnology

As technology delves into the netherworld of the nano, it enters with deference into a world in which biology has been innovating for eons. This is the realm of the building blocks of nature. It is here where technology hopes to intrepidly mesh with biology. This is nanobiotechnology. Nanobiotechnology will facilitate biological discovery and will inspire and integrate with technology at the nanoscale level.

Organisms are made of cells that are typically 10 μm in diameter. The organelles of the cell are even smaller, typically less than one micron, and smaller still are the proteins, RNA, and DNA whose dimensions are approximately a few nanometers. This is how big the smallest manmade nanoparticles are.[11a] In order to understand the inner workings of the cell, it is desirable to probe into the cell while minimizing disturbance. Pulled glass capillaries with nanoscale tips, carbon nanofibers, and fluorescent nanocrystals have so far been used as nanoscale intracellular probes.[20a]

Biological materials such as nucleic acids, enzymes and whole cells have been integrated into devices and systems to form novel electronic, optoelectronic, and memory devices for sensing and computation.[11a, 19a] One such device, the bioluminescent bioreporter integrated circuit (BBIC) couples bioluminescent *escheria coli* (e. coli) bacteria to a photosensitive IC for use as a chemical detector.[19a]

Technology is also being inspired by biology. Technology has a history of mimicking nature.[14a] Planes mimic birds, submarines mimic whales, cameras mimic

eyes, microphones mimic ears, and wires mimic nerves. These imitations rarely take the form of their progenitor, but attempt rather to mimic their function, sometimes with great success. Technology still has a great deal to learn from nature however. For example, the genome of the e. coli bacteria consists of 4300 base pairs which is equivalent to 9.2 Mb memory. The bacteria can exist in a range of harsh environments with extreme pH levels, temperatures, and salinities. It can perform a myriad of complex chemical operations to adapt to its environment, and it is self-assembling and self-replicating. All of these functions are integrated into a 2 square-micron area.[19a] Current technology can does not yet have this level of functionality, but it desires to mimic it using materials with which it is already familiar.

1.7 The Cell

One of the aspects of the cell that enables it to perform all of these functions in such a small space is in fact its size. As in micro- and nanofluidics, certain physical phenomena are enhanced at small scales. Their small size allows for molecular processing by simple, diffusion based mechanisms. Within the small volume of a cell, small changes in molecular numbers result in significant changes in concentration leading to altered reaction conditions.[7a] It has been suggested that cells use “macro-molecular crowding” as a means of regulating reaction rates by both limiting diffusion and increasing thermodynamic activity.[21a] To further facilitate function, the cell employs nanoscale structures such as organelles, and co-localized enzymes that enable metabolic processing.

Crucial to the vitality of the cell is the cell membrane, which plays a fundamental role in the creation of compartmentalized environments where activity occurs. The cell membrane is a semi-permeable fluid filled lipid bilayer that envelops the cell. It both contains and controls the chemical reactions within the cell. Reagents are exchanged through nanopores on the membrane surface by way of diffusion, which is a fast process due to its nanometer thickness. It is a challenge to engineering to mimic the small-scale functionality of the cell. In order to meet this challenge, it is necessary to develop a microfluidic nanoporous membrane (NPM) in the image of a cell membrane.[7a]

1.8 Artificial Cell Membrane

This thesis describes the design, fabrication and testing of two microfluidic structures with imbedded nanoporous membranes. Part 2 discusses the need for such devices, the engineering challenges that must be met, and a review of related projects. Part 3 describes a classical hydrodynamic model of such a device composed of carbon nanofibers. Part 4 describes a refined model utilizing fractals percolation theory. Part 5 describes the construction and testing of the device, conclusions, and Part 6 describes future work. My contributions to this project include: the design and fabrication of the device, the application of several mathematical models to the device in order to predict its behavior, the development of image processing software to analyze scanning electron micrographs in order to apply those models, the testing of the device, the development of image processing software to analyze that data, and the modification of the device with other materials to further enhance its performance. There are several ideas that are unique to this thesis. The first is that tortuosity, defined as a particle's path length

divided by its displacement is what scales the reference diffusion. The second is that the membrane can be thought of as a realization of some random fractal. The third is that tortuosity can be related to the resistance scaling factor, a property of a fractal. To support these claims I show a close agreement between a classical and a fractal permeability model. The fourth is that I incorporate a model to approximate surface effects. This shows that the surface cannot be categorically neglected because of the rather large device dimensions. The fifth is the extrapolation of 3-dimensional information from an SEM image used to determine the parameters that fit into the models. The sixth is the unique use of materials in this project.

Bibliography 1

[1a] R. P. Feynman, *There's Plenty of Room at the Bottom: An Invitation to Enter a New Field of Physics Engineering and Science*, Caltech, Feb. **1959**.

[2a] *Transistorized!* ScienCentral, Inc., and The American Institute of Physics, **1999.**

[3a] M Bellis , *Inventors of the Modern Computer: History of the Integrated Circuit-Jack Kilby and Robert Noyce.* http://inventors.about.com/library/weekly/aa080498.htm.

[4a] *Expanding Moore's Law: The Exponential Opportunity 2002 Update*, Intel.

[5a] D. M. Cannon Jr., T. Kuo, P. W. Bohn, and J. V. Sweedler Anal. Chem. **2003,** 75.

[6a] R. Barry and D. Ivanov *Journal of Nanobiotechnology* **2004,** 2, 2.

[7a] B. Fletcher, E Hullander, A Melechko, T McKnight, K Klein, D Hensley, J Morrell, M Simpson, and M Doktycz, *Nanoletters*, **2004,** 4, 10.

[8a] Jessamine M.K.Ng, Irina Gitlin, Abraham D.Stroock, George M.Whitesides *Electrophoresis* **2002**, 23, 3461.

[9a] L. Mazzola, *BizInk*. *Nanotech meets biotech in Silicon Valley*, **2003.**

[10a] R Jackman, T Floyd, R Ghodssi, M Schmidt and K Jensen *J. Micromech. Microeng*. **2001**, 11.

[11a] OV Salata *Journal of Nanobiotechnology* **2004**, 2, 3.

[12a] I Whamley *Nanotechnology*, **2003,** 14.

[13a] Whiteside, G., *nature biotechnology*, **2003**, 21, 10.

[14a] Madou, Marc, STM, July 25, 2003 The Impact of MEMS and NEMS on Biotechnology and Electronics in the 21st Century.

[15a] MICROLITHOGRAPHY From Computer Aided Design (CAD) to Patterned Substrate, Cornell Nanofabrication Facility, **2002.**

[16a] H Cao, Z Y Jian Wang, Jonas O. Tegenfeldt, Robert H. Austin, Erli Chen Wei Wu, and Stephen Y. Cho Ap Phys Lett, **2002,** 81, 1.

[17a] E. A. Coffman, A. V. Melechko, D. P. Allison, M. L. Simpson, and M. J. Doktycz. *Langmuir* **2004**, 20, 20, 8431.

[18a] Baum, R., *Nanotechnology: Drexler and Smalley make the case for and against 'molecular assemblers'* December 1, **2003**, 81, 48.

[19a] Simpson, M.L., Sayler G.S., Fleming J.T., Applegate B.*Trends Biotechnology* **2001** Aug;19, 8, 317-23.

[20a] McKnight, T. E. *et al Nanotechnology*, **2003,** 14**,** 551–556.

[21a] Ellis, R. J. TRENDS in Biochemical Sciences Vol.26 No.10 October **2001.**

[22a] K. E. Peterson, *Proc. IEEE,* **1982**, 70, 420.

2 Integrated Chemically Active Nanoporous Microfluidic Membranes

2.1 Benefits of Artificial Membranes

Technology can benefit in many ways from the development of NPMs because they can be used in a wide array of applications that require high surface area relative to other fluidic components. For example, thermodynamically, they can be used as high heat flux micro heat exchangers and micro jet arrays for cooling, and also for micro fuel cells.[1b] Their greatest potential is probably in the chemical and biological fields. They can aid in biochemical separations by molecular weight, size, charge, partition coefficient, or bioaffinity,[2b,3b,4b] They can allow for the retention of bio-macromolecules in micro total analysis systems.[4b,1b] They can be used for dialysis or the clean-up of biological samples prior to their introduction into a microfluidic network to help prevent clogging.[5b,6b,4b] They can be used to aid in the research of natural cell membranes and the intracellular dynamics of natural cells.[1b,7b,8b]

2.2 Three Important Qualities of Artificial Membranes

There are three important factors mitigating the production of NPMs. These are integrality, chemistry, and geometry. In order for the NPM to reach its full technological potential, all of the components of the analytical system in a microfluidic network must be miniaturized and integrated into a single device.[9b, 2b] In other words, the membrane must have a high degree of integrality. This means that the membrane would ideally be produced using techniques that are compatible with microfabrication and micromachining so it can share the intrinsic benefits of MEMS. Self-assembly is a compatible technique that greatly facilitates integrality. It should be noted that a

convenient side effect of using the techniques of microfabrication is that the membrane can be electrically addressed for ionic transport or electrochemical deposition.

It is also important to consider the chemistry of the membrane structure and the system in which it is contained. Methods must be developed to make the systems biocompatible and robust.[7b] Biological samples are very sensitive to issues such as hydrophobicity and the homogeneity of the materials used to build the microstructure in which they are confined.[10b] It may therefore be necessary to chemically passivate the structure to make it biocompatible. Inorganic compounds such as silica or organic molecules such as BSA can be adsorbed or chemisorbed on the surface of the membrane to make it inert.[2b] It may also be desirable to afford the membrane chemical selectivity by adsorbing other molecules to its surface. Often, an additional layer of linker molecules is required to proceed with further functionalisation.[12b]

The geometry of the membrane must also be taken into consideration. The pore size of the membrane must be tightly controlled with little variance over the membrane surface allowing precise molecular sieving and forcing interaction with chemically selective molecules bound to the pore.[3b] This means the pores should be approximately a few nanometers in diameter. A membrane with a high pore density is also desirable since it would allow for higher volumetric flow rates and facilitate diffusion if the surface chemistry allows for it.[10b] The membrane should also be thin, less than one micron, to facilitate diffusion and flow.[7b]

2.3 Engineering Challenges

In creating microfluidic NPMs with these ideal features, there exist two challenges: creation of sealed fluidic channels and reduction of pore diameter and thickness. Current sealing techniques such as wafer bonding,[10b] soft elastomer sealing (PDMS),[10b,2b] and photoepoxy sealing [14b] provide an effective seal for large planar surfaces. Wafer bonding requires a flat surface, and elastomer sealing suffers from clogging due to soft material intrusion into the channels.[10b] Some of the other properties of PDMS may prove deleterious in certain situations. For example, PDMS may cause features to shrink or sag. In addition, PDMS suffers from incompatibility with many organic solvents. Nonspecific adsorption may also occur. Methods to control the surface chemistry of PDMS are being currently being developed to overcome this problem.[2b] It is also difficult to form permanent bonds with PDMS seals, which reduces its efficacy in the large-scale manufacture of integrated devices. SU-8 has been used to seal microfluidic structures. SU-8 is compatible with standard microfabrication techniques, and does not require high temperature sealing. SU-8 can tolerate surface defects, and its softness during sealing can be temperature controlled, eliminating the problem of sagging and clogging. The seal is permanent, and if the microchannels are also defined in SU-8, then the sealed structure is chemically homogeneous. This is desirable for electro-osmotic flow regimes. Some unreacted epoxy groups may be present on the surface of the channel and available for further derivitization.[11b]

Currently, most commercially available membranes are made of organic polymers. Organic membranes are often not compatible with the fabrication of glass or

silicon devices because the high temperatures required to seal the devices will destroy the membranes. Organic membranes can be easily integrated into PDMS [2b] and SU-8 systems. These filters are not micromachined and typically have deviations in pore size that are not acceptable for critical biomedical applications such as virus removal and immunoisolation. Nanotechnology may provide a solution for both mass production and precision pore size control either by way of nanolithography or self-assembly.[13b]

2.4 Prior Art

There have been many attempts to construct microfluidic NPMs with varying degrees of success. A myriad of techniques have been developed and the following is a critique of the most important ones, reviewed in light of the above three design principles. It should be noted that some of these techniques were not intended to be used for the production of NPMs, but employed enough of the design principles to be considered as avenues of NPM research.

2.4.1 Lipid Membranes

Natural cell membranes are composed of lipid bilayers, so an obvious method of mimicking cell membranes is to use lipids. Many lipid systems have been used including liposomes [15b], lipid vesicles, black lipid membranes, Lang-muir-Blodgett layers and supported lipid bilayers, especially composed of phospholipids (SPBs).[8b] One supported bilayer actually extracts membranes from live cells and tethers them to an IC. Geometrically and chemically, they perform like lipid membranes because they are. Unfortunately, lipids are fragile structures and are difficult to precisely engineer with present technology.[7b] For this reason, they have low integrality.

2.4.2 Micromachined Membranes

The first submicron filters were developed by Kittilsland et al. using a traditional micromachining approach. They combined sacrificial oxide removal and a boron etch-stop to fabricate pores as small as 20 nm ± 10%. The membrane was successfully tested with 44 nm and 100 nm beads with only one defect in 10^7 pores.[16b] A microdialysis needle has also been fabricated using a sacrificial oxide technique to exclude large molecular weight compounds, and to sample interstitial fluids. Microneedles are integrated with other on-chip components such as flow channels, electronics, micropumps, microvalves, and a planar biochemical sensor. The pore size is approximately 30 nm.[5b] The sacrificial oxide technique shows high integrality and the potential for chemical functionalization, but suffers from a 5 μm thick membrane, low pore density (one pore in the case of the microneedle) and relatively large pore size.

2.4.3 Ion Track Etched Membranes

Nanopores have been fabricated in microfluidic devices *in situ* using a combination of micromachining and ion track etching. Microfluidic devices were constructed lithographically in polyimide, and were irradiated with heavy ions to form pores. The pores were opened with 2-N Sodium Hypochlorite. The devices were characterized by passing beads of varying diameter through the membrane and detecting their concentration at the output. This filter retained beads larger than 515 nm.[4b] Pores as small as 200 nm in diameter have been produced using ion track etching. These membranes were prefabricated in polycarbonate and sandwiched between PDMS microchannels. Electrokinetic flow of a sample plug was observed across the membrane.

These devices have some integrality since they rely on some traditional fabrication techniques, but the membranes are not directly electrically addressable and require PDMS sealing which is problematic in the large scale production of integrated devices. Chemical functionalization may be possible and the pore density is high, but the membranes suffer from being ten microns thick, and having large pores.

2.4.4 Laser-Induced Phase-Separation Polymerized Membranes

Laser-induced phase-separation polymerization of a porous acrylate polymer has been used for the *in situ* fabrication of dialysis membranes inside glass microchannels. A shaped 355 nm laser beam is used to define polymer membranes of 4-14 μm thickness, which bond to the glass microchannel and form a semipermeable membrane.[6b,18b] The membrane's pore size was measured to be less than 200 nm by the diffusion of latex microspheres. The dialysis membranes reported here are hydrophilic and show essentially no protein adhesion.[18b] These devices have some integrality since they rely on some traditional fabrication techniques, but the membranes are not directly electrically addressable. Chemical functionalization may difficult since proteins will not adsorb to its surface. The pore density may be high, but the membranes suffer from being too thick, and having large pores.

2.4.5 Nanoimprint Lithographic Membranes

Arrays of nanofluidic channels were fabricated using nanoimprint lithography (NIL). The NIL mold was generated by interferometric lithography (IL} and has 200 nm period grating. The minimum feature size of the nanochannels generated by IL is limited by the 100 nm wavelength of the light used for exposure. After NIL and etching, a

nonuniform deposition was used to both reduce the cross section of the nanochannels and seal the channels forming the pores. This process produced 10 nm pores. This process has high integrality and it could potentially be chemically functionalized. The sealing technique eliminates many problems associated with other soft elastomer sealing and wafer bonding while streamlining the fabrication process.[10b] The pore size is small enough at 10 nm for the sieving of macromolecules; the only possible drawback is that the pores or channels are aligned side by side in a single plane. It would take stacking many of these on top of one another to form an effective membrane, so the pore density is low.

2.4.6 Block Copolymer Template Method for Producing Membranes

Block copolymers form self-assembling nanostructures. The ability of soft materials such as block copolymers to form a rich variety of nanoscale periodic patterns offers the potential to fabricate high-density arrays for use in data storage, electronics, molecular separation and for combinatorial chemistry and DNA screening. Block copolymer films have already been investigated in several nanolithographic-etching processes, where the block copolymer functions as a self-assembling mask (SAM) to form nanopores with feature sizes as small as 10 nm.[19b] Like NIL, block copolymers provide a template for patterning nanostructures such as nanoporous membranes. Unlike NIL, these pores can be in a two-dimensional array so the pore density would be high. The chemistry would depend on the material that was patterned. This has great potential as a fabrication technique.

2.4.7 Colloidal Crystal Template Method for Producing Membranes

A template method of forming a nanoporous polypyrrole film was developed.[13b] Opalescent silica colloidal crystals made of 238 nm silica beads were self-assembled on SnO_2 coated glass by an evaporation method. After the sample was dried, polypyrrole was electrochemically deposited onto the silica spheres. HF was used to dissolve the beads leaving a polypyrrole film with spherical voids or pores. The pore size could be controlled by varying the voltage during pyrrole deposition.[13b] In this paper, the membrane was not integrated into a microfluidic system, but it could be done. It is also self-assembling, easing the fabrication process. Chemical functionalization of polypyrrole has been shown. The pores are three-dimensional, densely packed, and, although these pores are large (200 nm), smaller beads are commercially available. This process shows promise, but needs further development. Incidentally, colloids have also been used as SAMs.

2.4.8 Carbon Nanotubes as Membranes

Arrays of aligned carbon nanotubes (CNTs) were incorporated into a polymer film. The tips and the substrate were etched away to form a well ordered NPM. Varying the size of the catalyst particle can control pore size. Transport is through the core of the nanotube. The inner core diameter is 4.3 ± 2.3 nm. This is in the size range of many proteins and other important biological macromolecules. Transport measurements of both gas (N_2) and aqueous ionic species (Ru (NH3) $_6$ 3+) were performed to demonstrate transport through the inner cores of the CNTs. The open tips of CNTs with carboxyl end groups were readily functionalized, forming the basis for “gate keeper” controlled

chemical separations. The biotin/streptavidin analyte/receptor system was chosen to functionalize the membrane. With the attachment of the biotin tether, the $Ru(NH_3)_6^{3+}$ flux was reduced by 5.5 times. The ionic flux was further reduced by a factor of 15 upon streptavidin coordination with biotin.[3b] This process has the potential for integrality, though it has not been demonstrated, and CNTs are self-assembling. It could possibly be integrated into layered systems such as the ion tracked and laser-induced structures. Chemical functionalization has been demonstrated. The size of the pores is very small and the pore density is very high. This process shows great promise, but needs further development.

2.4.9 Vertically Aligned Carbon Nanofibers as Membranes

Dense arrays of vertically aligned carbon nanofibers (VACNFs) have been used to form microfluidic NPMs. The array was grown to a height of about 2.5 μm by PECVD from a photolithographically defined 50 μm wide nickel stripe. Microchannels were replica molded in PDMS and laid over the VACNF array to form a membrane structure. The effective pore size was determined to be 500 nm by flowing successive sizes of fluorescently labeled latex beads through the membrane.[22b] This process has some integrality since VACNFs are self-assembling, and they were defined using photolithography. The use of PDMS is, however, problematic for the large-scale fabrication of integrated devices. The fibers are readily biochemically functionalized.[7b] This structure suffers from having soluble microchannels of photoresist reducing its biochemical efficacy and a detachable PDMS lid. The heterogeneous nature of the materials also makes it difficult to use with electro-osmotic

flow. Although the pores are densely packed, at 500 μm wide the pores are large, at 50 μm, the membrane is thick, and at 2 μm high, the channels are shallow. This process, however, has promise because of its integrality and robustness. It can readily be combined with some of the other techniques above described.

Bibliography 2

[1b] *Changgu Lee and Luc G. Fréchette*, Proceedings of IMECE'02 2002 ASME International Mechanical Engineering Congress & Exposition New Orleans, Louisiana, November 17-22, 2002.

[2b] Jessamine M.K.Ng, Irina Gitlin, Abraham D.Stroock, George M.Whitesides *Electrophoresis* **2002**, 23, 3461.

[3b] Bruce J.Hinds, Nitin Chopra, Terry Rantell, Rodney Andrews, Vasilis Gavalas, Leonidas G.Bachas *Sciencexpress* November **2003.**

[4b] S Metz ,C Trautmann,A Bertsch, and Ph Renaud *J. Micromech. Microeng*. **2004**, 14.

[5b] Jeffrey D. Zahn, AjayA.Deshmukh, Alexandros P. Papavasiliou, Albert P.Pisano, and Dorian Liepmann Proceedings of 2001 *ASME International Mechanical Engineering Congress and Exposition* November 11-16, 2001.

[6b] Brian J. Kirby and Anup K. Singh *In-situ Fabrication of Dialysis Membranes in Glass Microchannels Using Laser-induced* Phase-Separation Polymerization Sandia National Laboratories, Livermore, CA.

[7b] B Fletcher, E Hullander, A Melechko, T McKnight, K Klein, D Hensley, J Morrell,| M Simpson, and M Doktycz, *Nanoletters*, **2004,** 4, 10.

[8b] B. Seantier, C. Breffa, O. Fe´ lix, and G. Decher *Nanoletters*, **2004**, v4, 1.

[9b] Bing He, Li Tan, and Fred Regnier, *Anal. Chem.***1999**, 71, 1464.

[10b] H Cao, Z Y Jian Wang, Jonas O. Tegenfeldt, Robert H. Austin, Erli Chen Wei Wu, and Stephen Y. Cho Ap Phys Lett, 81, 1, **2002.**

[11b] R Jackman, T Floyd, R Ghodssi, M Schmidt and K Jensen *J. Micromech. Microeng*. 11 **2001** 1–8.

[12b] I Whamley *Nanotechnology*, **2003,** 14.

[13b] Takayuki Sumida, Yuji Wada, Takayuki Kitamura and Shozo Yanagida *Chem. Commun.,* 2000.

[14b] Madou, Marc, STM, July 25, 2003 The Impact of MEMS and NEMS on Biotechnology and Electronics in the 21st Century.

[15b] W Vreeland and L Locascio 7th International Conference on Miniaturized Chemical and Biochemical Analysts Systems October 5-9, **2003**, Squaw Valley, California USA.

[16b] Wen-Hwa Chu, Ruby Chin, Tony Huen, and Mauro Ferrari *J. MEMS*, 8, 1, **1999.**

[17a] E. A. Coffman, A. V. Melechko, D. P. Allison, M. L. Simpson, and M. J. Doktycz. *Langmui,r* **2004**, 20, 20, 8431.

[18b] Simon Song, Timothy J. Shepodd, Anup K. Singh, and Brian J. Kirby 7th International Conference on Miniaturized Chemical and Biochemical Analysts Systems October 5-9, 2003, Squaw Valley, Callfornla USA.

[19b] I Whamley *Nanotechnology*, 14, **2003.**

3 Microscale and Nanoscale Fluid Mechanics: A Classical Approach

3.1 Pressure Driven Flow in Channels

At large scales, fluid dynamics are explained by a set of equations developed in the nineteenth century independently by Navier, Stokes, Poiseuille, Darcy, Hagen, Knudsen, and Reynolds among others.[1c,2c,3c,4c,5c,6c] These models describe the velocity of fluids in a channel as functions of position, pressure, friction constants, density, and the geometry of the channel. These equations are very useful when applied to the design of hydrodynamics and serve as the archetype for modeling microscale flow regimes. There are two kinds of flow with respect to viscous and inertial forces, turbulent and laminar. Turbulent flow streams have eddies and vortices caused by the inertia of the fluid and viscosity. Laminar flow streams are dominated by viscous forces and are smooth and independent of the surface roughness of the flow channel. To determine whether flow in a fluidic channel will be laminar or turbulent, a dimensionless number called the Reynolds number is calculated. The Reynolds number can be thought of as the ratio of inertial forces to viscous forces.[3c, 5c, 4c] For Reynolds numbers greater than about 2000, turbulent flows occur, while laminar flows occur at lower Reynolds numbers. Reynolds number is defined by

(1)

$$\mathrm{Re} = \frac{\rho \nu_{ave} \delta}{\eta},$$

where ρ is the density of the fluid, ν is the average velocity, δ is the hydrodynamic diameter of the channel, and η is the dynamic viscosity of the fluid. For water, ρ is 1 g cm^{-3}, and η is 0.0114 $cm^{-1}s^{-1}$.[3c, 4c, 5c] So the Reynolds number is typically very small,

much less than 2000, for typical velocities in microfluidic channels and hence the flow in these channels is usually laminar. Under laminar flow conditions, the fluid can be thought of as concentric cylinders of constant velocity that slide over each other.[3c, 4c, 5c] The friction between those layers is called viscosity. Laminar flow has a parabolic velocity profile in cylindrical channels, where flow is quickest in the middle of the channel and is zero at the inner surface of the channel.[1c, 2c, 5c, 8c] The velocity, *v*, of a cylinder of fluid at a position α from the center of the pipe is given by

(2)

$$v(\alpha) = v_{\max}\left(1 - \frac{\alpha^2}{r^2}\right)$$

and

(3)

$$v_{\max} = \frac{r^2}{4\eta}\left(-\frac{dp}{dx}\right).$$

Here, *r* is the hydrodynamic radius of the channel, v is the velocity of a layer of fluid, η is the dynamic viscosity, *p* is pressure, and *x* is axial position along the pipe. Integrating over the cross section of the channel gives the volumetric flow rate, Φ, as

(4)

$$\Phi = \frac{1}{2} v_{\max} \pi r^2 .$$

Combining 2, 3, and 4 gives Poiseuille's Equation. This manipulation assumes that the relationship between length and pressure drop is linear. The Poiseuille Equation is

(5)

$$\Delta p = \frac{8\eta L\Phi}{\pi r^4},$$

where L is the length of the pipe.[2c, 5c, 7c] The flow resistance, R_c, of a microfluidic channel is defined as the ratio of the pressure drop,ΔP, to the flow rate, Φ,

(6)

$$R_c = \frac{\Delta P}{\Phi}.$$

From 5,

(7)

$$R_c = \frac{8\eta l}{\pi r^4}$$

where η is viscosity, l is the length of the channel and r is the radius of the channel. For rectangular channels this equation has to be modified.

(8)

$$R_c = \frac{2f\,\mathrm{Re}\,\eta l}{ab\delta^2}$$

where f Re is a friction constant, a and b are the width and height of the rectangular channel, and δ is the hydrodynamic diameter given by

(9)

$$\delta = \frac{2ab}{a+b}.$$

[2c, 5c, 8c] For example, for water in a 10 μm x 50 μm channel, the resistance per unit length is r_c=1*10^{13} g s cm^{-3}.

The pressure difference along a length of channel can also be expressed in terms of the Darcy friction factor, *f*.

(10)

$$\Delta p = f \frac{L}{2R} \rho \frac{u_{ave}^{\ 2}}{2}.$$

By setting 10 equal to 5, solving for *f* and comparing to 1, it can be shown that

(11)

$$f \, \mathrm{Re} = C$$

where *C* is defined as the friction constant. This relationship has been well established experimentally at the macroscale, but for microchannels this constant becomes a function of the channel dimensions.[3c, 4c, 5c, 7c, 8c]

3.2 Pressure Driven Flow through Porous Media

When many microfluidic channels are connected into a network, a porous material is formed.[5c, 8c] Thin porous materials are called membranes. It is possible to find the equivalent resistance of this network by summing all of the individual components of the network, but many porous materials are disordered and approximating this network would be arduous. Also, it is difficult to predict how fluids will behave in microfluidic channels as will be discussed later,[4c, 8c, 9c] so it would be even more

difficult to predict the behavior of fluids in a network of these channels. For this reason, another quantity is used to characterize flow through porous materials. Permeability is a porous material's resistance to pressure driven flow and is described by Darcy's Law,

(12)

$$\Phi = \frac{\kappa \Delta P A}{\eta L},$$

where again Φ is the volumetric flow rate, ΔP is the pressure across the membrane, A is the cross sectional area, η is the dynamic viscosity, L is the length of the membrane, and a friction constant, κ, is the permeability.[6c,10c,11c] The resistance to fluid flow, defined by 6, of the porous membrane is then given by rearranging 12,

(13)

$$R_m = \frac{\eta L}{\kappa A}.$$

3.3 Permeability of Ordered Media

Assuming the membrane material is ordered, simple expressions can be derived for the permeability by finding the equivalent flow resistance of the network of channels composing the membrane. Tsay and Weinbaum [12c] have found from the Stokes-Brinkman model [11c,23c,12c] for porous materials composed of regularly spaced (**ordered**) vertically aligned fibers, an exact solution for the permeability is given by

(14)

$$\kappa = .0572 r_f^{\,2} \left(d / r_f \right)^{2.377}.$$

Curry and Michel [11c,6c] have found that the permeability of a fibrous membrane is given by

(15)

$$\kappa = \frac{3}{4} r_f^{\,2} \left(\frac{1-\phi}{\phi} \right)$$

In 14 and 15, r_f is the mean radius of the fibers, d is the inter-fiber spacing, and ϕ is the volume fraction of the fibers.[11c,13c,14c] Figure 3.1 shows a surface plot of the normalized resistance of a fibrous membrane against fiber volume fraction and fiber radius. As can be seen, small variations in the nanoscale dimensions of the fibers produce large variations in the normalized resistance.

3.4 Determination of Permeability from SEM Images

The parameters ϕ and r_f, and hence the permeability, κ, can be approximated by analyzing scanning electron microscope (SEM) images of real membranes. Further, it can be shown that there is a relationship between the position in the grayscale of a pixel and the position along the *z*-axis in certain classes of SEM images. This means that a top-down view will yield three-dimensional information about the geometry of the material under investigation. This can be seen in Figure 3.2. This triptych shows two SEM images of the same VACNF membrane installed in a microfluidic channel. In the first panel, the tilt is zero degrees from the normal of the substrate and in the second panel, the tilt is thirty degrees from the normal. The third panel was generated letting the brightness in the grayscale be equal to a position on the z-axis at every position in the x-y plane. A wire mesh of the structure was then rendered at a thirty-degree tilt from the normal axis.

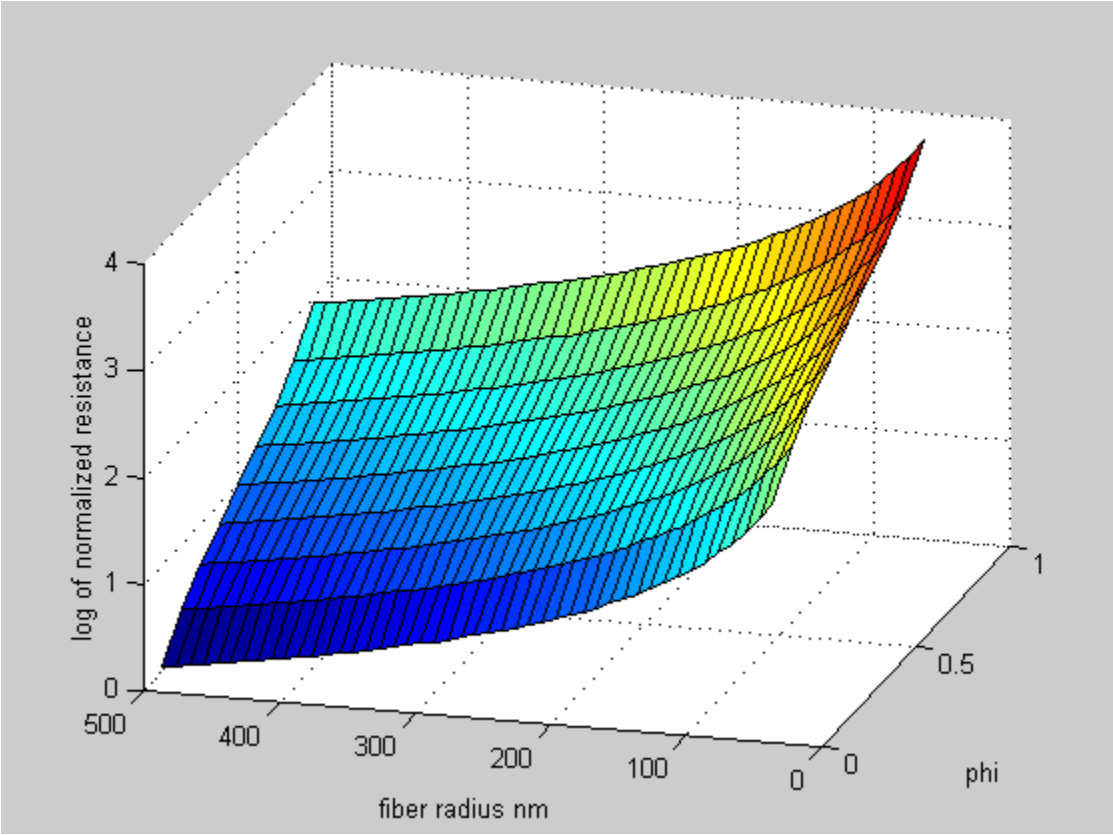

Figure 3.1 Surface Log Plot of Normalized Resistance versus Fiber Radius and Fiber Volume Fraction. As can be seen, the resistance of a fibrous membrane is highly sensitive to variations in fiber radius.

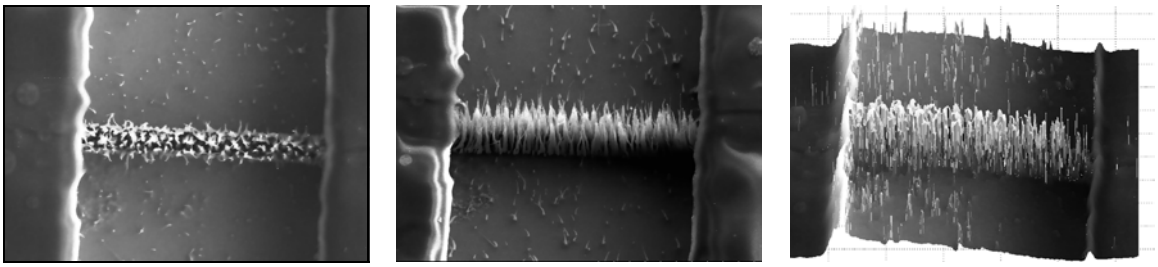

Figure 3.2 Fiber Triptych. The left panel shows a top down view of a VACNF membrane in a microfluidic channel. The middle panel shows the same structure at a 30º pitch. The right panel shows a structure rendered at a 30º pitch from the three dimensional grayscale information in the top panel. Note the high degree of similarity between the middle and right panels.

By comparing analogous features in panels two and three, it can clearly be seen that a correlation exists between the brightness of a pixel in panel one and the height of the structure at that location. This is useful because it allows one to calculate the permeability of a material whose fibers are irregularly shaped by summing in parallel the resistance of each plane. This relationship is peculiar to this type of material. Because the fibers are homogeneous, taller fibers have more surface area to scatter electrons and appear brighter than shorter fibers. Because the fibers are vertically aligned, taller fibers do not block the view of shorter underlying features. Field enhancement at the tips of the fibers is a source of error in this measurement causing the sharp nickel points to appear brighter and hence taller than they actually are.

To characterize the fluidic properties of a VACNF membrane, an image processing algorithm was developed and is given in Appendix 4. The algorithm takes a grayscale SEM image of a VACNF membrane and converts it to a black and white image as can be seen in Figures 3.3A and 3.3B. This was done by setting a threshold in the grayscale above which pixels would be made white, and below which they would be made black. The algorithm counts the number of fibers in the image by scanning the image until a white pixel was found representing the edge of a fiber. All adjacent pixels were marked and a counter was then incremented. The algorithm proceeds until it finds another white pixel or a marked pixel and again marks all adjacent pixels. If the white pixel is adjacent to a marked pixel, then the fiber was already counted and the fiber count is not incremented, otherwise the counter is incremented. Once the fibers ;asldkja; have

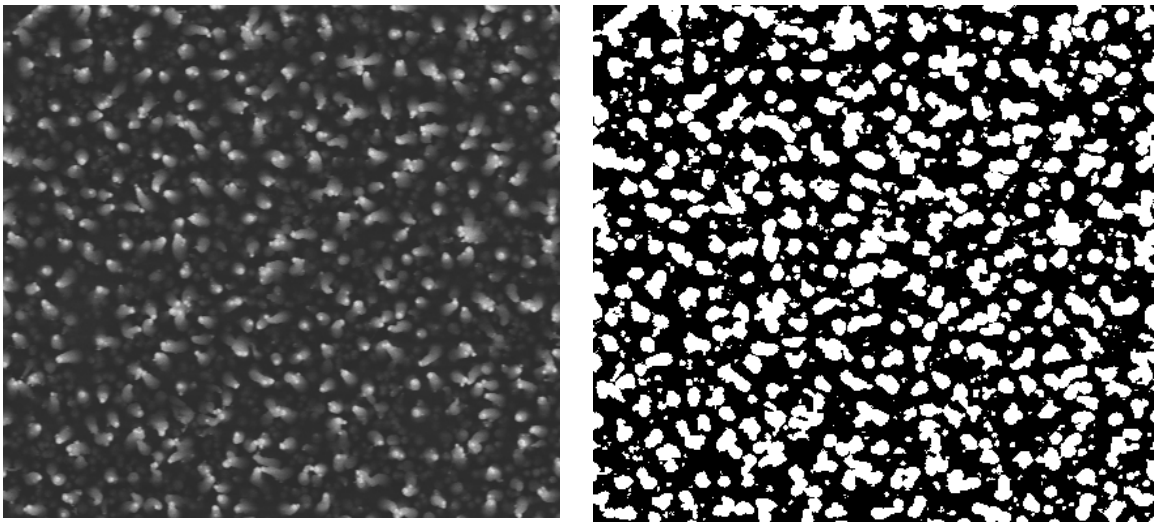

A B

Figure 3.3 Binary Fibers. The left panel shows an SEM image of a carbon nanofiber membrane. The right panel shows a binary rendering of the same membrane.

been counted, the algorithm sums all of the white space to give the total fiber area. This area was divided by the fiber count to give the average fiber area, and hence the average fiber radius. These values are then used in Equations 13, 14, and 15 to give the effective permeability, pore diameter, and resistance of the VACNF membrane at the given grayscale threshold and hence at every plane in the membrane. The algorithm iteratively characterizes the fiber membrane at all thresholds in the range of the grayscale where fibers could be resolved. These can be are added in parallel to give the total resistance of the channel.

3.5 Hydrodynamic Properties of VACNF Membranes

Assuming we have accurately quantified the membranes resistance, the total resistance of a network composed of microfluidic channels and nanoporous membranes can calculated by the series and parallel combination of these elecments. For example, the total resistance of a microfluidic circuit consisting of a membrane intalled in a microfluidic channel of equal size is given by

(14)

$$R = R_c + R_m$$

Table 3.1 gives the results of the analysis of the VACNF membrane in Figure 3.2A. Figure 3.4 shows a plot of the calculated fiber and pore diameter at all altitudes in the membrane. These dimensions seem to be consistent with measurements made by hand of SEM images of VACNF membranes. It should be noted that the standard deviations

Table 3.1 Hydrodynamic Properties.

	Mean		Standard Deviation	
Fiber Population Density	285	±	130	Mfibers cm^{-2}
Porosity	0.835	±	0.12	
Effective fiber radius	150	±	9	nm
Effective Pore diameter	1.0	±	0.3	μm
Effective Permeability	1.36e-9	±	0.94e-9	cm^2
Normalized Resistivity	13.4	±	N/A	

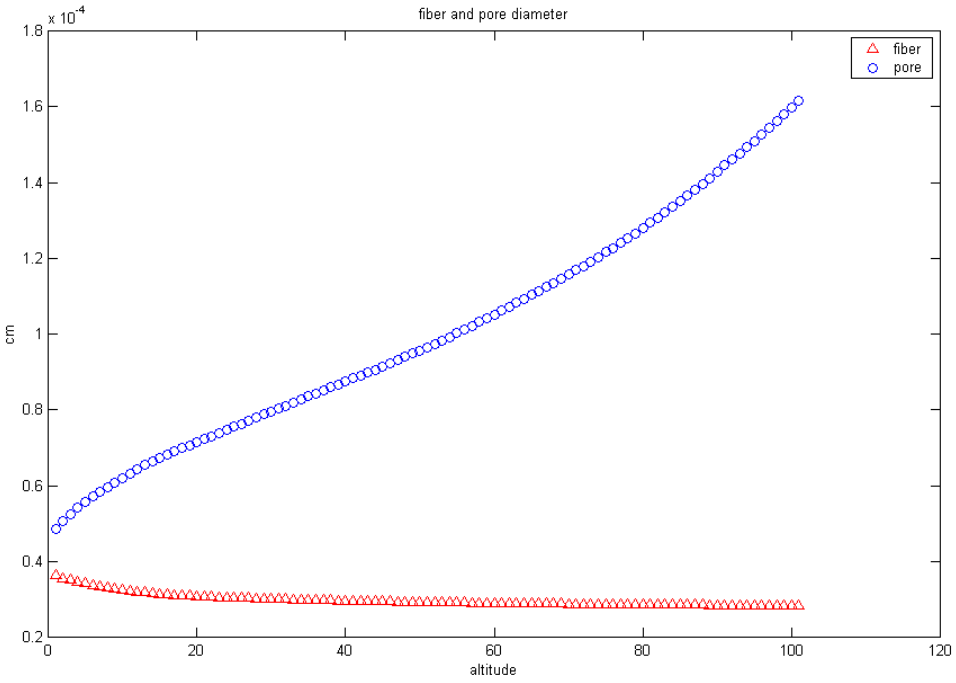

Figure 3.4 Hydrodynamic Pore Diameter. The red line represents the fiber diameter. The blue line represents the mean pore diameter calculated in the previous part.

given represent variations in the **effective** parameters at different heights in the membrane, and do not represent variations in the **individual** parameters. Some interesting things to note about these values are the rather small standard deviations in porosity and fiber radius, and the rather large standard deviations in population, pore diameter, and permeability. This implies that the fibers are very nearly cylindrical and that the porosity does not change much from bottom to top. The fibers membranes are mostly open space as suggested by the high value for the porosity, and there is a steady decrease in population with altitude. The pore diameter was computed by substituting the values for porosity and fiber radius into 14 and rearranging. The exponential dependence of the pore diameter on these parameters yielded large variations in pore size at different altitudes in the membrane. The same can be said for the variations in permeability. After summing in parallel the resistances of all of the planes, the total resistivity of the membrane was found to be only 13.5 times greater than the resistance of the open channel, but as was illustrated in Figure 3.1, this measurement depends on the accuracy of the image processing algorithm.

3.6 Diffusion

Another dynamic fluidic process besides the collective flow of material is diffusion. Diffusion is a thermodynamic process where the particles of two or more fluids intermingle with one another. Fick's second law of diffusion describes how the concentrations of fluids change in space and time. In the first dimension it is given by

(20)

$$\frac{\partial N(x,t)}{\partial t} = D \cdot \frac{\partial^2 N(x,t)}{\partial x^2}$$

where D is the constant of diffusivity, N is the concentration of a solute at a position, x,and at a time, t, in the channel. [15c,10c] The process this model describes will be referred to as bulk-diffusion. Traditionally this is the only type of diffusion accounted for in hydrodynamic models. There are at least two types of diffusion however, self-diffusion, and bulk-diffusion.[5c,16c,17c] Self-diffusion is due to molecule-surface interactions. The reference diffusivity, D_{os}, for self diffusion is given by

(21)

$$D_{os} = \frac{1}{3}\bar{u}\, d\ .$$

where $\bar{u}$ is the average particle velocity and d is the mean intercept length to a wall.[4c,18c,19c,17c] For infinitely long cylindrical pores, d is the diameter of the pore. Bulk-diffusion is due to molecule-molecule interactions. The reference diffusivity, D_{ob}, for bulk-diffusion is given by

(22)

$$D_{ob} = \frac{1}{3}\bar{u}\,\lambda$$

where λ is the mean free path of a gas molecule, or the lattice spacing of a liquid.[4c,18c,19c] Einstein [20c, 21c] showed that D_{ob} is related to the mean-squared displacement of a brownian particle in time according to

(24)

$$\left\langle l^2 \right\rangle = 2dD_{ob}t$$

where d is the Euclidean dimension t is time and l is displacement. This is known as normal diffusion. The total reference diffusion in a cylindrical pore [16c,17c] is given by

(25)

$$\frac{1}{D_o} = \frac{1}{D_{os}} + \frac{1}{D_{ob}}.$$

Clearly,

(26)

$$\lim_{d\to 0} D_o = D_{os} \text{ and } \lim_{d\to \infty} D_o = D_{ob}.$$

3.7 Diffusion in Disordered Media

The expressions for the reference diffusions assume that particles are free to diffuse in any direction and do not interact with any other macro-molecules except for the wall of the pore space. In 1948 Pollard and Present showed that if particles are forced to diffuse within the maze-like confines of a porous material, the total diffusivity, D, is given by

(8a)

$$\frac{1}{D} = \frac{\tau_s}{D_{os}} + \frac{\tau_b}{D_{ob}},$$

where τs and τb are the self and bulk tortuosities.[16c, 17c] These numbers characterize how twisted the path of a particle is through a porous medium. Tortuosity is defined as the ratio of curvilinear path length between two points and the straight-line distance between the same two points. It has traditionally been assumed that the two tortuosities are equal since both self-diffusing particles and bulk-diffusing particles of equal size weave approximately the same path through a membrane on average. Ogston et al.[11c,14c] found that

(28)

$$\tau_b = A \exp\left(\frac{r_s + r_f}{r_f} \phi^{\frac{1}{2}} \right)$$

for a **disordered** fibrous membrane, where r_s is the radius of a diffusing particle, c is the weight per volume concentration of the solute, and A is a constant between 1 and 0.75 that weakly depends on the membrane geometry.[11c, 22c]

3.8 Diffusion through VACNF Membrane

It is not explicitly stated in his paper that this factor is the tortuosity. Instead it is a factor used to multiply the reference diffusivity, defined in 22, to give the diffusivity D in 8a for a fibrous membrane. Since this factor performs the same function as the tortuosity, it is equivalent to the tortuosity. If we assume the tortuosities for both self and bulk diffusion to be equal in the VACNF membrane, the pore diameter, d, is sufficiently

large, approximately 1 μm, to neglect self-diffusion. Substituting this value for d into Equation 8a with λ=0.3 nm predicts that self diffusion would only acount for about 0.03% of the total diffusion, but further investigation will show that this may be an oversimplification. Using the above calculated values for fiber radius and porosity, the diffusive characteristics of the membrane pictured in Figure 3.3A can be calculated. Figure 3.5 shows a log plot of the normalized diffusion coefficient computed from the Ogston model for the fibrous membrane in Figure 3.3A. This plot assumes *A* is unity. As can be seen from this plot, the diffusivity begins to decrease rapidly for particles with a diameter greater than 100 nm. The lower boundary corresponds to diffusion at lower altitudes in the membrane while the upper boundary corresponds to diffusion at higher altitudes. These bounds were computed from the standard deviations of the bulk-tortuosity factor.

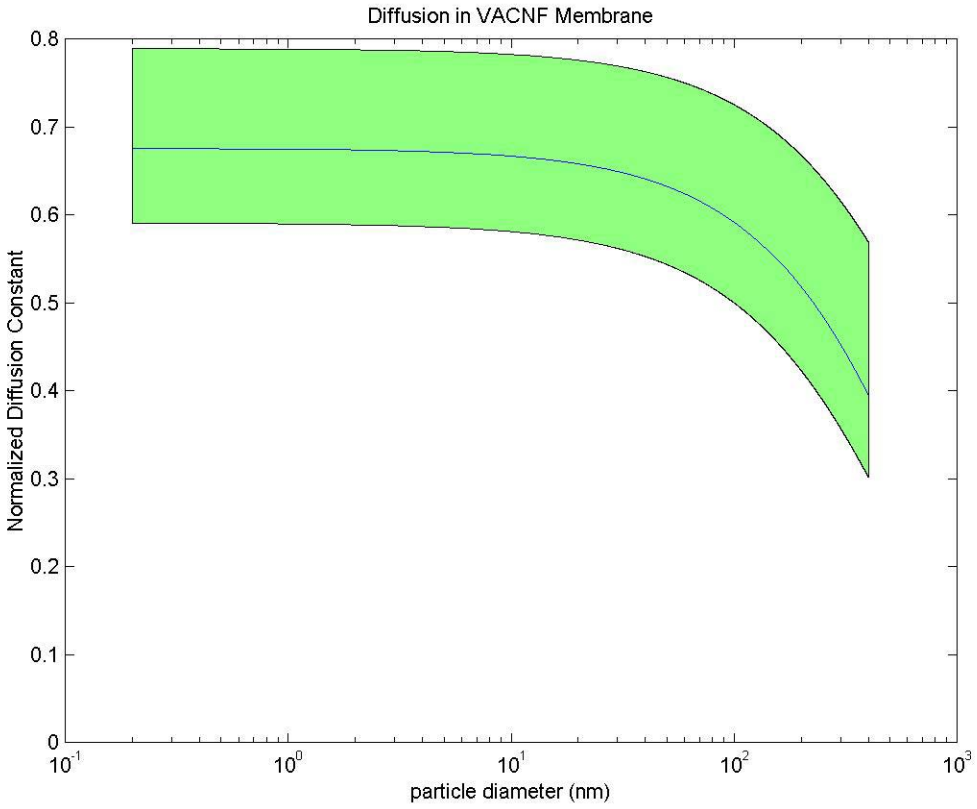

Figure 3.5 Normalized Diffusion Constant versus the Particle Diameter. The lower boundary represents diffusion at the base of the fibers while the upper boundary represents diffusion at the tips. The blue line is the mean.

Bibliography 3

[1c] C. L. M. H. Navier, Mem. *Acad. R. Sci. Inst. France*,**1823**,1, 414.

[2c] Poiseuille, M., *CR Hebdomaires des Seances Acad. Sci.* **1848** 11.

[3c] Reynolds, O., *Phil. Trans. R. Soc. London* **1883** 2, 51.

[4c] Mohamed Gad-el-Hak (ed), *The MEMS Handbook*, CRC Press, 2002.

[5c] E. M. Purcell, Am. J. Phys. **1977**, 45, 3.

[6c] Curry, F. E., and C. C. Michel.. *Microvasc Res* **1980**, 20, 96.

[7c] M Elwenspoek; T S J Lammerink; R Miyakei; J H J Ruitman; *J. Micromech. Microeng*, **1994** 4, 28a.

[8c] C Ho Y Tai, *Annu. Rev. Fluid Mech*. **1998**, 30, 579.

[9c] Mohamed Gad-el-Hak, *J. Fluids Eng*., **1999**, 5, 121.

[10c] From C Hall and W D Hoff, *Transport in brick, stone and concrete*, **2002**.

[11c] Nuen, *Biophys J*, **1999**, 77, 1, 542.

[12c] Tsay, R., and Weinbaum, S., *J. of Fluid Mechanics*, **1991,** 226, 67.

[13c] Jackson, G. W., D. G. James., *Can. J. Chem. Eng.* **1986,** 64, 362.

[14c] Ogston, A. G., *Faraday Soc. Trans.,* **1958,** 54, 1754.

[15c] C. T. Culbertson , *Talanta,* **2002,** 56 365.

[16c] W. G. Pollard and R. D. Present, *Phys. Rev*. **1948**, 73, 762.

[17c] Geier, Vasenkov, and Kärger , *J. Chem. Phys*., **2002**, 117, 5.

[18c] Probstein, RF *Physicochemical Hydrodynamics: An Introduction, second edition*, John Wiley & Sons, New York, 1994.

[19c] Bridgeman, PW, *Proc. Am. Acad. Arts Sci.* **1923,** 59, 141.

[20c] Einstein, A., *Investigations on the Theory of the Brownian Movement*, New York: Dover **1956**.

[22c] Phillips, R. J., W. M. Deen, and J. F. Brady.. *J. Colloid. Interface Sci*., **1990**, 139, 363.

4 Microscale and Nanoscale Fluid Mechanics: A Modern Approach

4.1 Hydrodynamic Properties of Disordered Media

In the preceding section, an image-processing algorithm was used to quantify the geometric properties of a membrane composed of vertically aligned carbon nanofibers (VACNFs). These characteristics were used in classical models to predict the permeability and diffusive characteristics of this membrane. While the diffusion models used assume a disordered media, the permeability models assume that the membrane is ordered with a regular lattice spacing and homogeneous when, in fact, the membrane is disordered and heterogeneous.[1d, 2d] The predictions made from these models should be thought of as first order approximations. The following will attempt to apply modern mathematical models widely used by geologists to study diffusion and permeation in disordered porous media. This should provide more insight into the diffusive and permissive behavior of VACNF membranes.

4.2 Percolation Models of Disordered Media

There are several works suggesting that fractal percolation models effectively account for the topologies inherent in disordered diffusive systems. Percolation theory is the mathematics of connectivity on discrete graphs, lattices, or networks. Percolation occurs when there is a connected path of conducting lattice sites spanning the entire lattice space. Such a connected path is called a percolation cluster. The percolation threshold represents the minimum number of conducting lattice sites to allow percolation to occur, and is related to the porosity of the lattice.[3d, 4d, 5d] Empirical studies have shown that for 2-dimensional infinitely ramified Bernoulli (uncorrelated) networks, the porosity at the threshold of percolation is 0.59. In other words, 59% of the lattice has to

be conducting to guarantee percolation. The network in Figure 4.1 is a Bernoulli network at the threshold of percolation.[3d, 4d] In 3-dimensions, only 31% of the lattice sites need to be conducting for percolation to occur.[3d, 4d, 5d, 6d] At the threshold of percolation, the percolation cluster becomes a *fractal* and exhibits *anomalous* diffusive behavior.

4.3 Fractal Models of Disordered Media

It has been observed that many disordered porous media are fractal-like; therefore understanding the relationship between diffusive transport on fractal graphs and the fractal dimension should provide insight into the diffusive nature of real porous media.[1d, 2d, 7d, 8d] A *fractal* is a structure that is self-similar across all length scales and obeys a *fractal* scaling law. This means that one or more of its *scalar* quantities, m, (e.g. volume, surface area, or length) scales with the resolution of the tool, b, used to measure it. The fractal scaling law is given by

(31)

$$m = b^{idf}$$

where df is the **fractal dimension**, b is the basis, and m is the scalar quantity after some number of iterations, i. The implication is that fractal dimensions are *in-between* Euclidean dimensions. Consider the object pictured in Figure 4.2. This is one of the

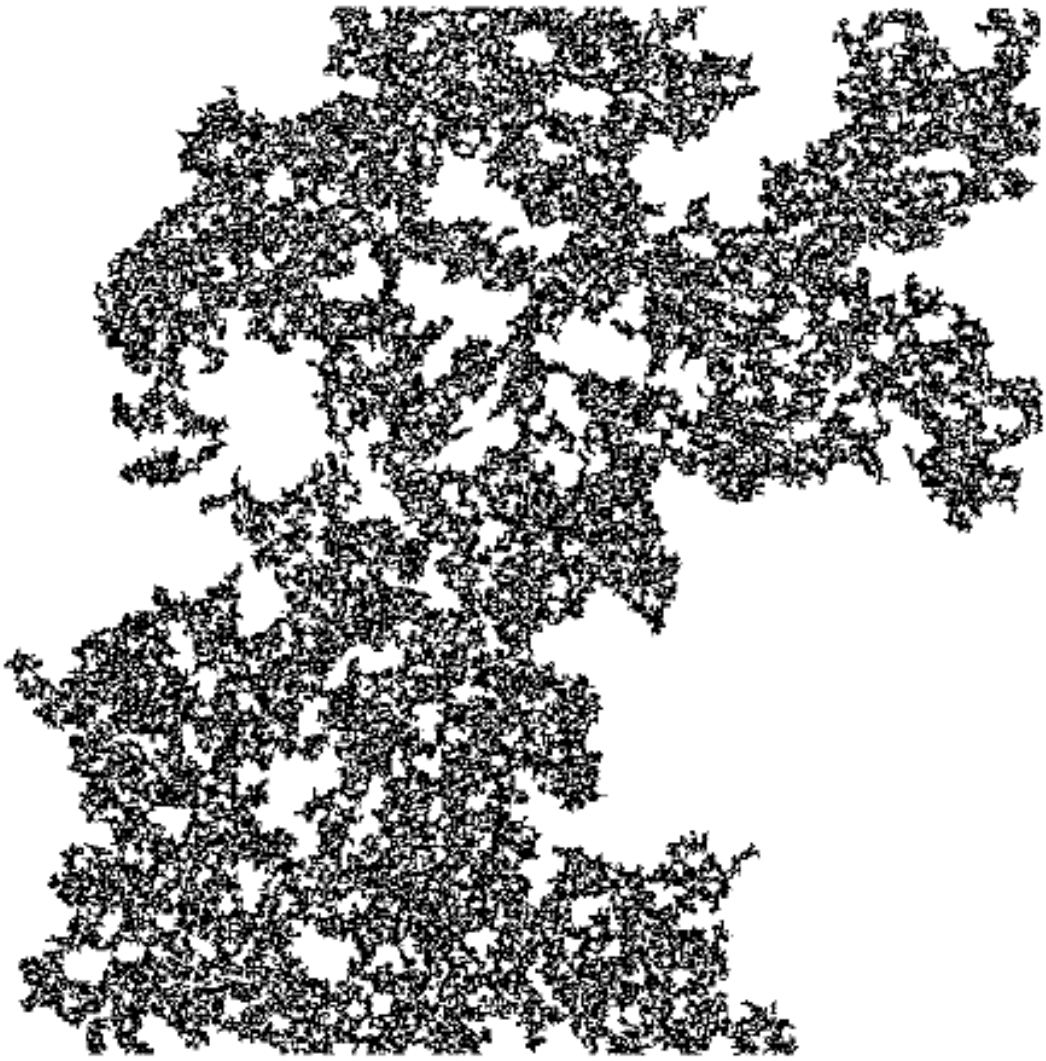

Figure 4.1 Bernoulli Lattice. *Df*=1.89, Reprint Courtesy Sukop et al. [4d]

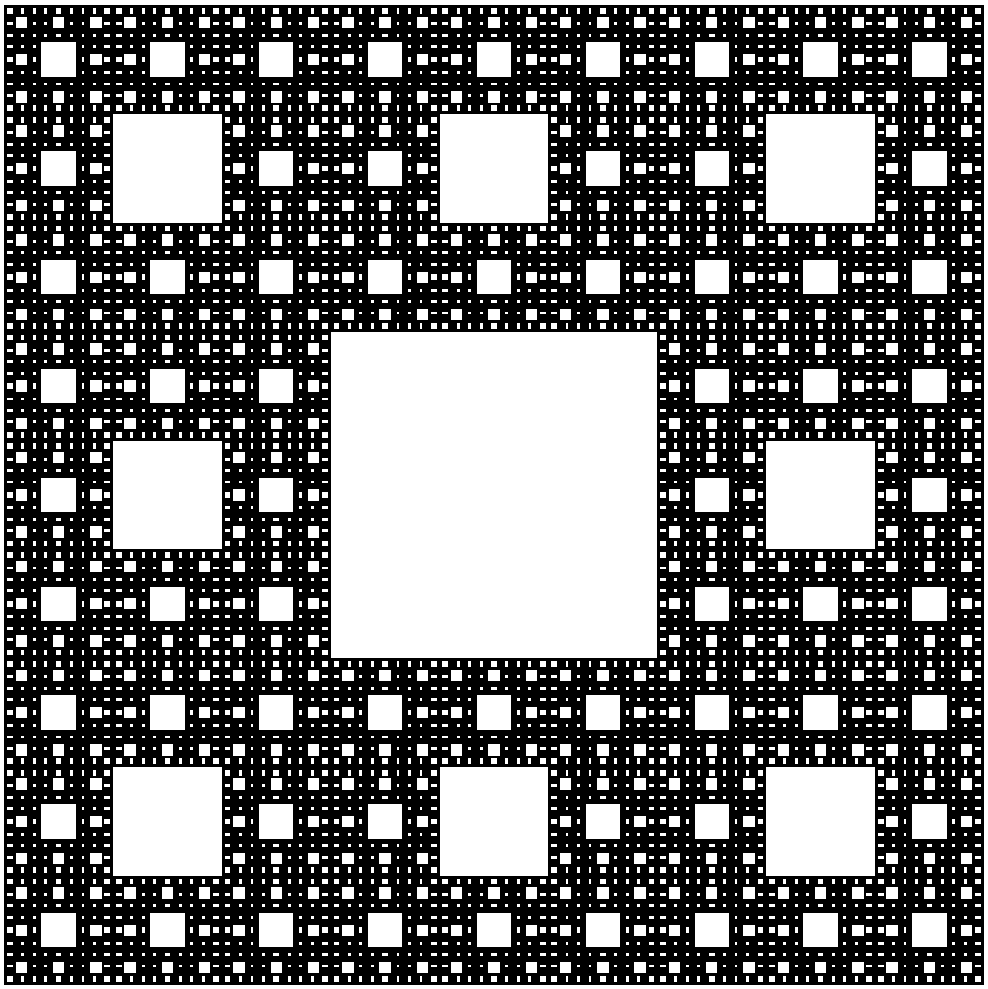

Figure 4.2 Sierpinski Carpet. *Df*=1.89

simplest fractals, known as the Sierpinski Carpet. The Sierpinski carpet has been used extensively in diffusion studies because its behavior mimics real disordered porous materials, and exact solutions exist for many of its transport properties. It is generated by taking an empty box and dividing it into a *b* x *b* grid. If *b* is three, then this produces nine smaller empty boxes of equal size. The middle box is filled. Each of the remaining 8 boxes is divided into a *b* x *b* grid, and each of their middle boxes is filled. This process is repeated *ad infinitum*. At the end of each iteration, *i*, there are *m* remaining empty boxes. Rearranging 31 gives the fractal dimension of the void space of a Sierpinski carpet.

(32)

$$df = \frac{\ln(m)}{\ln(b)}.$$

Note that if no boxes were filled at each iteration, then the object would be an empty plane and its fractal dimension, *df*, would equal 2, the Euclidean dimension. So, the Euclidean dimension is a special case of the fractal dimension when *df* is an integer. Figure 4.3 is an example of a random Sierpinski carpet.[9d] Random Sierpinski carpets are generated by randomly choosing which square to remove at each iteration in their generation. The fractal dimension of these carpets, however, is the same as their deterministic counterparts since *m* and *b* are the same.

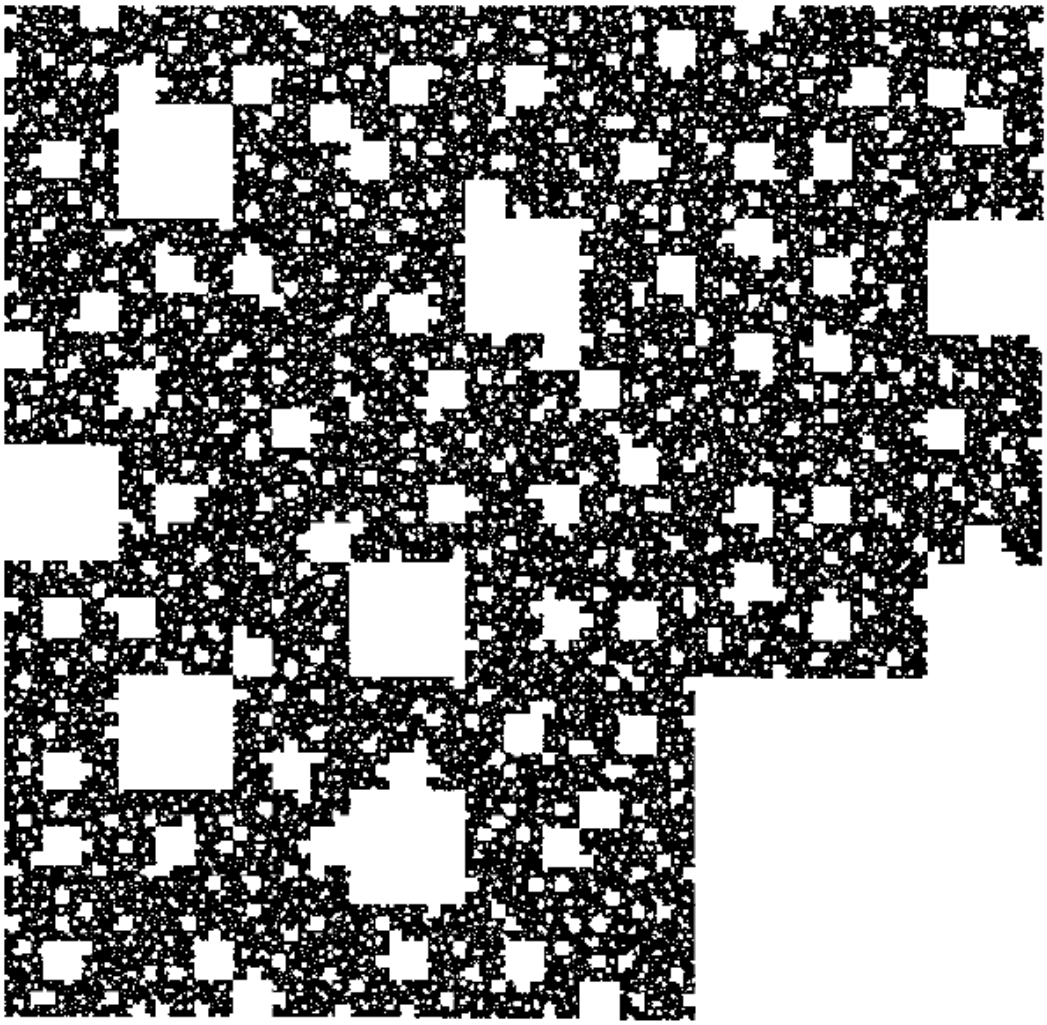

Figure 4.3 Random Sierpinski Carpet. *Df*=1.89 Reprint Courtesy Sukop et al. [4d]

4.4 Box Counting Algorithm

The fractal dimension of a real porous media can be determined graphically by applying the principle outlined above in reverse. This is commonly done using a box-counting algorithm. The algorithm counts how many boxes, m, of width, $1/b$, it takes to cover the pore space. The box size is modulated and a log-log plot of the box size versus the box count is made. If the pore space is truly fractal, this plot will be a straight line with an R2 value of 1, and whose slope is the fractal dimension. The panels in Figure 4.4 show a box-counting algorithm applied to a membrane composed of vertically aligned carbon nanofibers. Like the parameters determined in the previous parts, the fractal dimension also depends on the grayscale threshold and hence the altitude in the membrane, and therefore, box counting was performed at several altitudes in the membrane. Box counting was also performed on the mass space of the membrane to see if the mass space was fractal as well. This is important because mass fractals can have different transport properties than pore fractals. The R2 deviation was calculated along with the fractal dimensions of the mass and pore space. Figures 4.5, 4.5A and 4.5B shows the results from some of these tests. As can be seen, the pore space has a higher R2 value and hence is more fractal than the mass space. This was found to be the case throughout 80% of the membrane. In all cases the R2 value for the pore-space was very nearly one, so a fractal pore model should adequately approximate a VACNF membrane. Figure 4.6 shows a plot of the fractal dimension against altitude in the membrane.

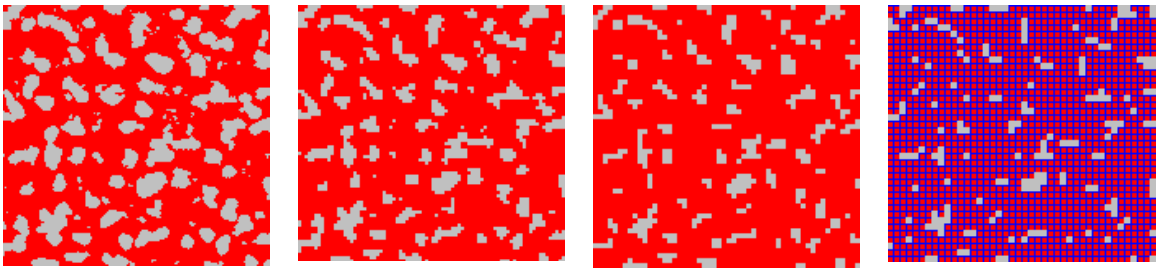

b=1	*b*=1/2	*b*=1/3	*b*=1/4
m=18089	*m*=5107	*m*=2472	*m*=1515

Figure 4.4 Box Counting. Box Counting algorithm applied to black and white image of VACNF membrane. Counting was performed on the pore space.

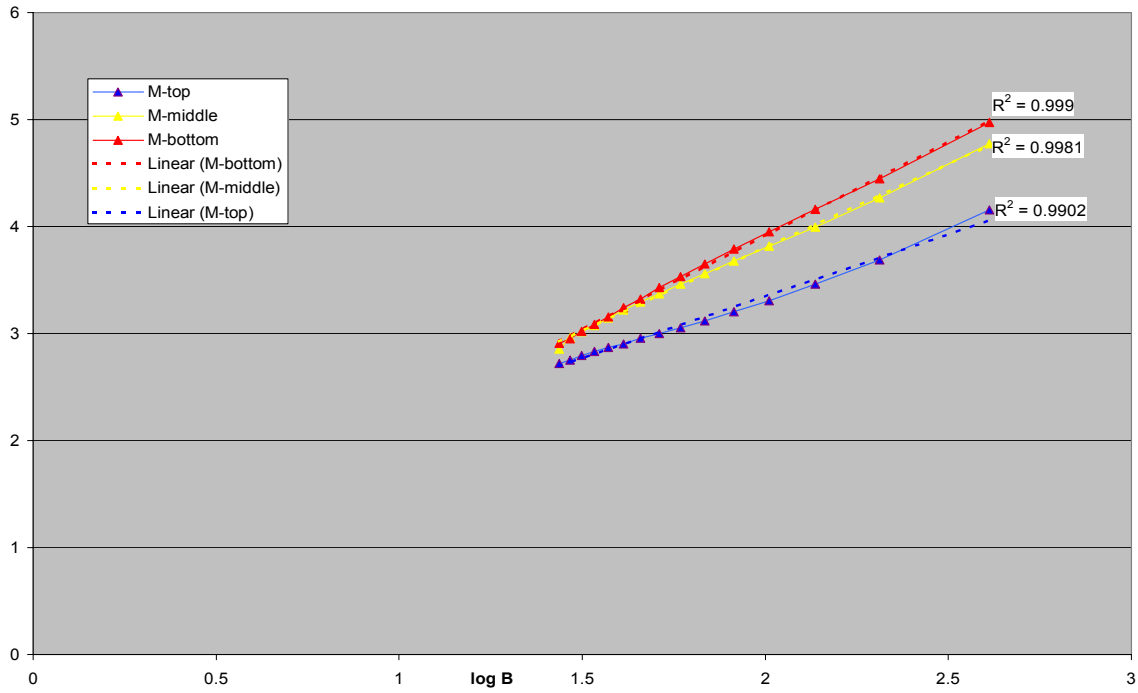

Figure 4.5. Log Plot of Box Count. A) On Mass Space.

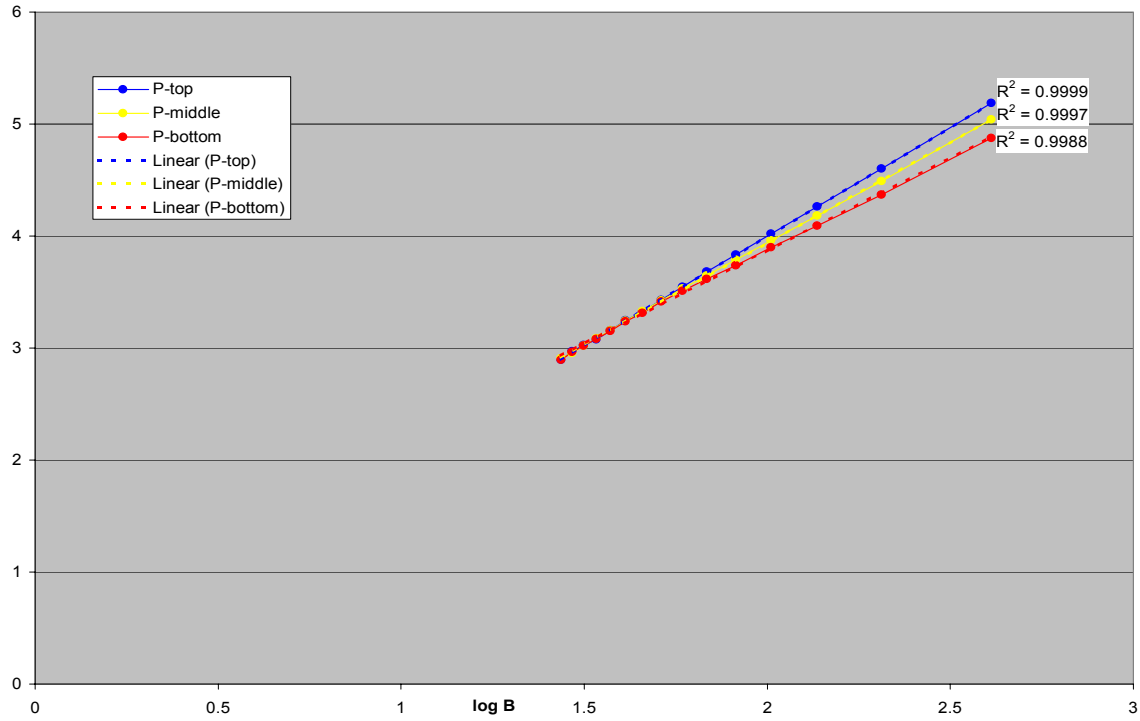

Figure 4.5. Continued. B) On Pore Space.

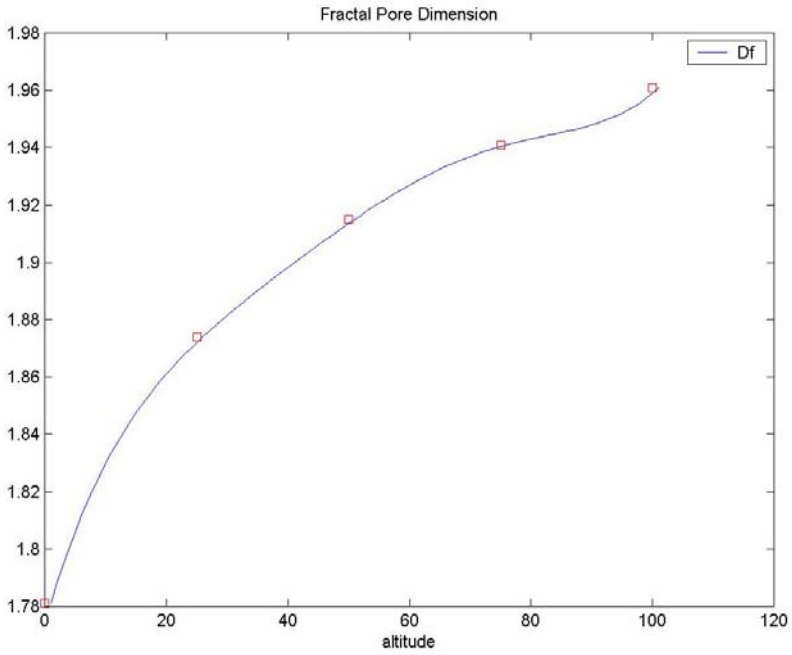

Figure 4.6 Fractal Dimension of Pore Space. Df is of a 2-D slice of VACNF membrane at varying altitudes.

4.5 Fractal Dimension Membrane Properties

In 1985 Katz and Thompson showed that the fractal dimension of a real porous media can also be determined from the pore size distribution and the porosity of the media. In the second Euclidean dimension, this is given by

(33)

$$df = 2 - \frac{\ln(\theta)}{\ln\left(r_o / r_m\right)}.$$

[8d, 10d, 11d, 12d]

where θ is the porosity, r_o and r_m are the minimum and maximum pore radii respectively, and *df* is the fractal dimension of the pore space. This equation holds exactly for exactly self-similar pore fractals such as a Sierpinski carpet, and holds approximately for real porous media. Inspecting this equation shows that as the pore-size distribution narrows or as the porosity increases, *df* approaches 2. As the porosity decreases or the pore-size distribution increases, *df* approaches 1. Hunt and Gee have recently verified this result experimentally.[8d] Rearranging this equation gives

(34)

$$df = \frac{\ln(\theta\left(r_m / r_o\right)^2)}{\ln\left(r_m / r_o\right)}$$

4.6 Sierpinski Carpet Approximation of VACNF Membrane

If we try to compare the graph of a real porous material to a Sierpinski carpet, then comparing Equation 34 to Equation 32 suggests we are using

(35)

$$b = r_m / r_o$$

and

(36)

$$m = \theta \left(r_m / r_o \right)^2$$

for the basis and for the mass of the pore space. If *df* is already known, or can be found using a box counting algorithm, then

(37)

$$b = \theta^{\frac{1}{df-2}}$$

and

(38)

$$m = \theta^{\frac{df}{df-2}} .$$

Figure 4.7 shows a plot of *b* and *m* versus height in a VACNF membrane. The values of *df* were computed using the box counting algorithm.

4.7 Anamolous Diffusion

Random walks, illustrating Brownian motion, are statistically self-similar and hence fractal. Equation 24 describing Brownian motion can be generalized for the case when Brownian particles are not free to diffuse in three dimensions, but are restricted to

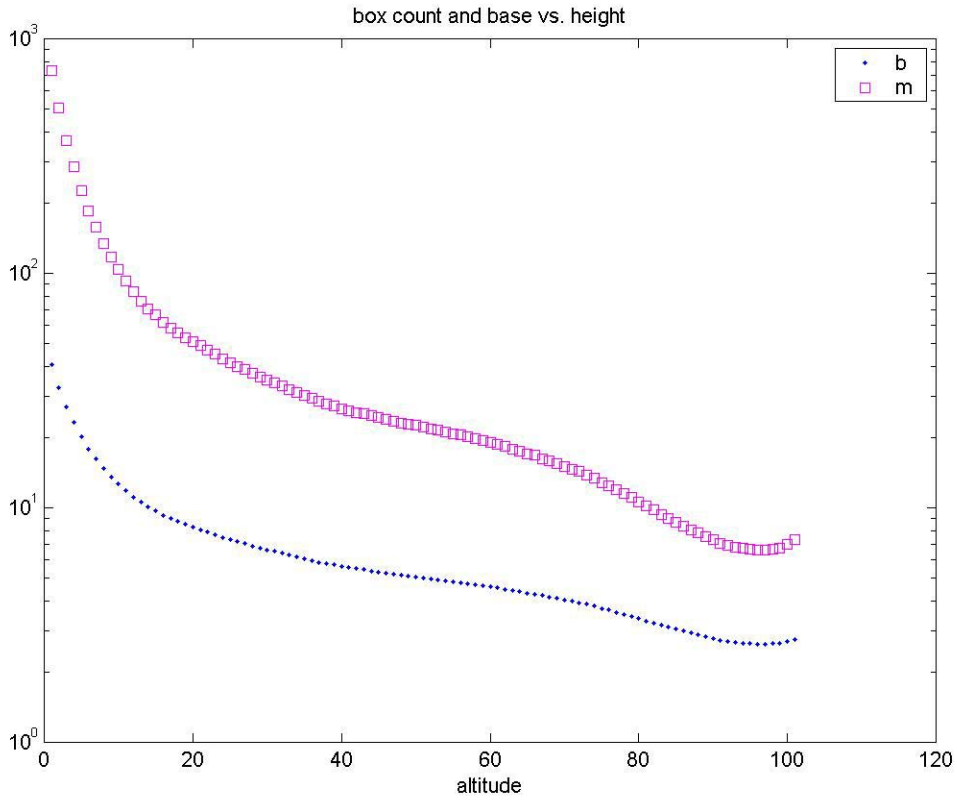

Figure 4.7 Sierpinski Realization. The Box Count was used to find *Df*. *Df* was then used in equations 35 and 36 to find *m* and *b* at all altitudes in the membrane.

the maze-like confines of a fractal graph. The mean squared displacement of a particle is given by

(39)

$$\left\langle l^2 \right\rangle \propto t^{\frac{2}{dw}}.$$

Here *dw* is the **fractal walk dimension**. When *dw* is equal to 2, normal-type Brownian diffusion is taking place as described by Equation 24. When *dw* is greater than 2, *anomalous* diffusion is taking place. As was stated earlier, percolation clusters at the threshold of percolation are fractal. Diffusion on these critical clusters has been shown to be anomalous.[2d, 5d, 13d, 6d, 14d, 7d, 15d]

If random walks are fractal and the graphs upon which the walks are taking place are fractal, then it is natural to inquire about the relationship between the fractal dimension of the graph, and the fractal dimension of the walk. One of the major problems in this field is a proof of the *fractal* Einstein relation relating diffusivity to permeability on all fractal graphs. Though a general proof of the fractal Einstein relation for all fractals does not exist, there is enough compelling evidence supporting the relation to assume that it is true. Proofs for special classes of fractals, such as the Sierpinski carpet, have been demonstrated [16d, 7d] and simulations of random walks on wide classes of fractals have shown that the Einstein relation holds for many other types of fractal graphs.[14d, 7d, 16d] Simple scaling arguments [6d] yield the fractal Einstein relation as

(40)

$$d_w = d_f + \zeta$$

Here, ζ is the resistance scaling exponent.[6d, 7d] The resistance scaling exponent is a parameter used to describe how the flow resistances, R, scales with the length scale of the porous material according to

(41)

$$R \propto l^{\zeta} .$$

Many attempts have been made to analytically determine the walk dimension. Kim et al. found that the upper and lower bounds for the walk dimension on random Sierpinski carpets are given by

(42)

$$dw^{upper} = \log\left[\left(\frac{b-l}{b} + \frac{l}{b-l}\right)\left(b^2 - l^2\right)\right]\left(\log b\right)^{-1}$$
$$dw^{lower} = \log\left[\left(\frac{b}{b-l}\right)\left(b^2 - l^2\right)\right]\left(\log b\right)^{-1}$$

where l is the side length of the squares removed at each iteration in the generation of the carpet.[17d] For Sierpinski carpets,

(43)

$$l = \sqrt{b^2 - m} .$$

Simulation results have varied. Kim's simulation fit within these bounds. Reis has also shown through Monte Carlo (MC) simulation that the walk dimensions, *dw*, of wide

arrays of randomly generated Sierpinski carpets of the same fractal dimensions are similar.[16d] Dasgupta, however, found a close match for the lower bound of the walk dimension in Equation 42, but a higher upper limit that approached *df*+1. They claim that the deviation from Kim's model may be due to a higher degree of symmetry in Kim's graphs.[18d]

Figure 4.8 shows a plot of the bounds of *dw* versus height in a VACNF membrane. The values of *m* and *b* used in equation 42 are shown in Figure 4.8. This model predicts diffusion will be slightly more anomalous at the base of the membrane than at the ceiling, but is very nearly 2 in all cases, and is therefore nearly normal type diffusion. This result is also predicted from percolation theory which suggests that normal type diffusion takes place on graphs whose porosity is above the percolation threshold.[4d, 2d] Figure 4.9 shows a plot for the bounds of ζ. These were calculated from equation 40, the fractal Einstein relation.

4.8 Fractal Permeability

Yu and Liu recently described a method for determining the permeability of a porous media from the fractal dimension of the pore space, *df*, the fractal dimension of the tortuosity, $d\tau$, and the maximum hydrodynamic pore radius. The fractal permeability is given by

(44)

$$\kappa_f = G\frac{L_o^{1-d\tau}}{A}\frac{df}{3+d\tau-df}\left(\delta_{\max}\right)^{3+d\tau}.$$

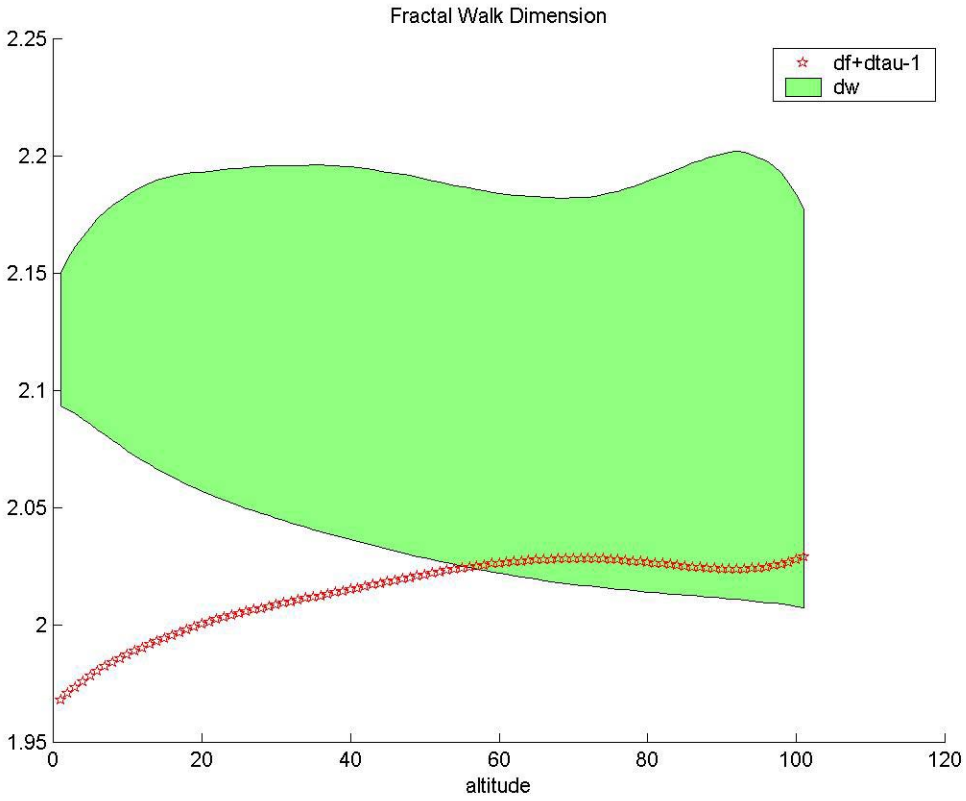

Figure 4.8 Walk Dimension. Diffusion in VACNF membrane is slightly anomalous at base of membrane with dw greater than 2. Dw was calculated using the values of b and m shown in Figure 4.8. The red line was calculated by assuming that a simple relationship exists between the fractal tortuosity dimension and zeta, and then applying equation 34.

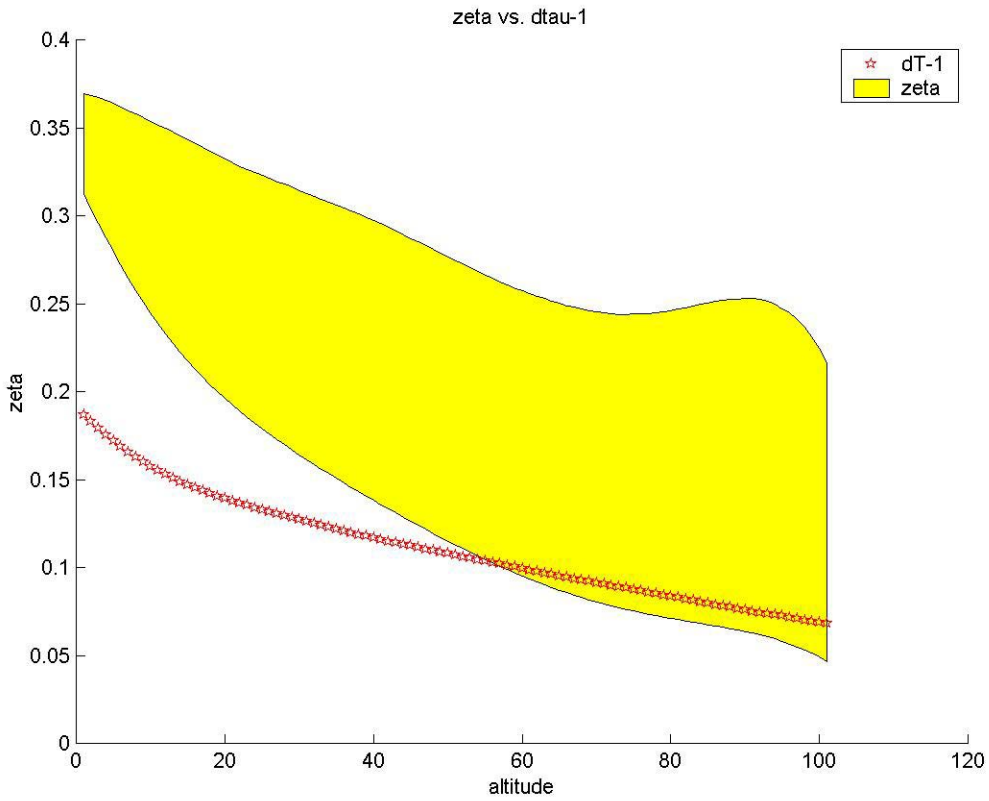

Figure 4.9 Zeta. Zeta was calculated by substituting the values for df and dw into Equation 40 and solving for zeta. The red line is the fractal tortuosity dimension-1.

Here, G is a constant, approximately $\pi/128$, L_o and A are the length and the cross-sectional area of the porous media respectively, and δ_{MAX} is the maximum hydrodynamic pore diameter [10d] which can be found from Equation 9. Again, one should note that here the critical dimension is the **maximum** pore diameter, and in the previous part, an average pore diameter was used to determine the permeability. Recall from the previous part that the ratio of a particle's path length to its displacement is called the tortuosity τ. The fractal bulk tortuosity, τ_{bf}, is given by

(45)

$$\tau_{bf} = \left(\frac{L_o}{\delta}\right)^{d\tau - 1}.$$

If this is equivalent to the bulk-tortuosity, τ_b, derived from the Ogsten model described by Equation 28, then we can solve Equation 45 for the fractal tortuosity dimension, and substitute into Equation 44 to obtain the fractal permeability. Setting Equation 28 equal to Equation 45 and solving for $d\tau$ gives

(46)

$$d\tau = \frac{\phi^{\frac{1}{2}}}{\ln\left(\frac{L_o}{\delta}\right)} + 1$$

Examining this equation shows that as the mass fraction decreases or the pores become long and thin, the $d\tau$ approaches 1. As the porosity decreases or the pores become short and fat, the $d\tau$ approaches 2. It can also be shown that $d\tau$ is related to ζ, the resistance

scaling factor. Resistance is a quantity that grows proportionally with length. If the length of a resistor obeys a fractal scaling law, then the resistance does as well and is described by Equation 41. In other words, if we multiply displacement by tortuosity, we have path length. If we multiply this by resistivity, we have resistance. If the tortuosity is fractal, so is the resistance with

(47)

$$\zeta = d\tau - 1$$

Figure 4.9 shows a plot of the resistance scaling factor calculated from the fractal Einstein relation and $d\tau$-1.

The permeability of a real disordered media can be determined from its length, width, height, porosity, mean fiber radius, and the fractal dimension of the pore space. In the preceding part, all of these parameters were used to determine the permeability and diffusivity of a real porous media with the exception of the fractal dimension. It was assumed in the permeability models that the media was ordered, implying their fractal dimension was equal to their Euclidean dimension. Also, in the previous part, it was assumed that normal-type Brownian diffusion was taking place. The above development accounts for all of the same geometrical properties of a porous media along with addition of a non-integer fractal dimension to account for the material being disordered. To account for the effects of disorder in the porous media on diffusion and permeation, it only remains to determine the real fractal dimension of the media. Using *df* in Equation 44 along with the values calculated for the mean pore radius from the previous part, we can now calculate the fractal permeability of the VACNF membrane. Since the

maximum pore diameter is not known, average pore diameter was used instead. We can assume then that the actual permeability is higher than the plots project. Once again these values were computed throughout the grayscale, and hence at all altitudes in the membrane. Figures 4.10 and 4.11 show the results of these calculations and the calculations from the preceding part. The red line represents the actual tortuosity calculated graphically with different values for the parameter A from the Ogsten model. The green line represents the idealized fractal model when the graph is a 2-D lattice, and the fractal tortuosity dimension is 1. The blue line represents the classical model. Note the close agreement between the fractal model and the classical model. This supports the validity of both the classical and the fractal models. The fractal model yields a slightly higher permeability that the classical model when the lattice is ordered. When we consider the tortuosity, the permeability in the fractal permeability is reduced slightly.

4.9 Nanofluidics

The dimension that characterizes in which regime a fluidic system is operating is the hydrodynamic diameter. The models for bulk fluid flow and diffusion described in the previous section have worked very well for hydrodynamic systems whose characteristic dimension is greater than one millimeter; however, for channels with microscale dimensions, these relationships begin to break down.[19d,20d,21d,22d] Recall that $f\,\mathrm{Re}$ should be a constant, C, according to the classical models. Figure 4.12 shows the results of several pressure driven flow experiments carried out in microchannels to determine the relationship between the friction factor and the Reynolds number where C^* is the normalized constant, given by

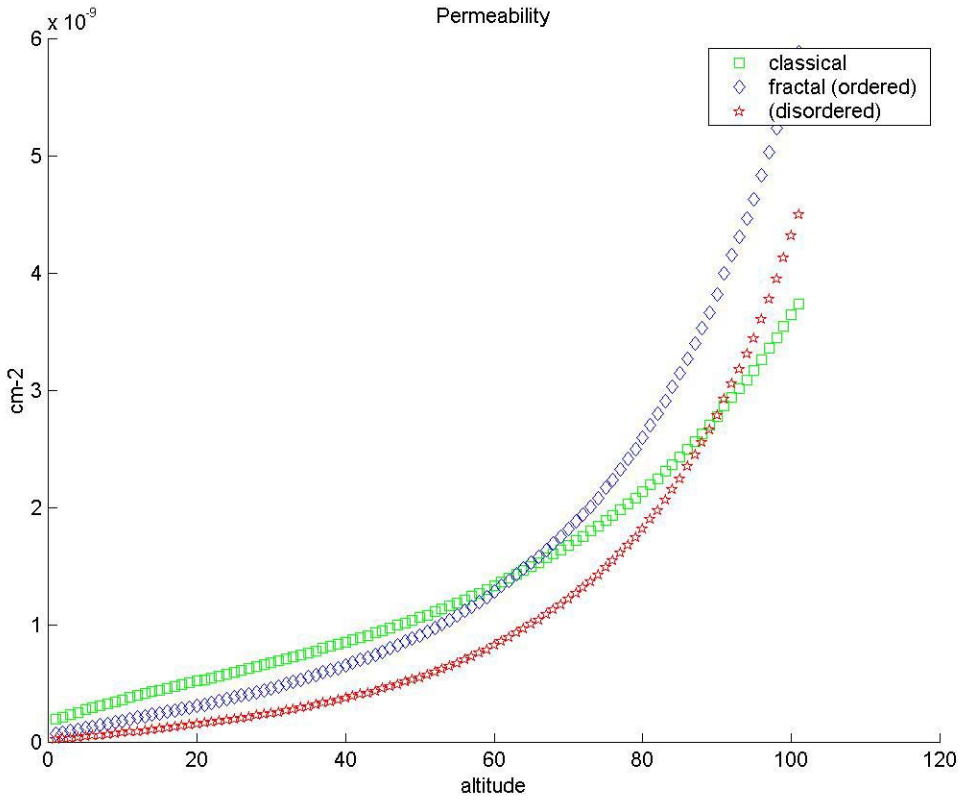

Figure 4.10 Permeability. The blue line was calculated from the Yu fractal model and assumes uniform pore size and spacing. The red line was calculated from the Yu fractal model, but df and dt were calculated from images of VACNF. The green line is the permeability from the Tsay-Weinbaum and Curry-Michel models described in the last part.

	Classical	Fractal (ordered)	Fractal (disordered)
Normalized Resistivity	13.4	11.9	17.23

Figure 4.11 Resistivity. By multiplying the permeability by a small rectangular area and integrating across all altitudes, the resistance can be calculated.

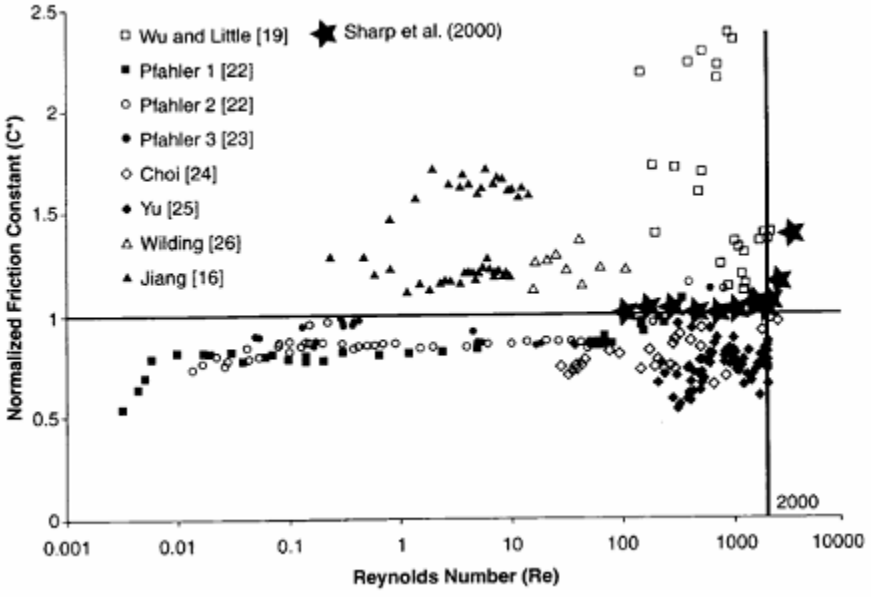

Figure 4.12 Plot of Normalized Friction Constant against Re. Reprint Courtesy [21d] Gad-el-Hak, *MEMS Handbook*.

(48)

$$C^* = \frac{C_{meas}}{C_{theory}}.$$

This Figure highlights the inefficacy of the theoretical fluid flow models when applied to microscale flow regimes. It is not clear whether these deviations are a result of experimental error, or they are the result of other physical processes that begin to dominate at small scales, or both. At the very least, they highlight the difficulty in engineering micro and nanofluidic structures. As can be seen from the plot, the friction constant deviates in both directions from the theoretical value for Re > 0.1. For Re < 0.1, the friction constant is consistently less than the predicted value.[19d,20d,21d,22d] One phenomenon that is not accounted for in the classical models is the effect of the surface. Experiments have shown that hydrophilic flows over hydrophobic boundaries can allow for a surface-slip velocity that is 10% of the maximum bulk velocity in microchannels. This is in violation of the no-slip boundary condition tacitly assumed in Equation 2, and is negligible for systems whose characteristic dimension is greater than 1mm.[32,33,19d,20d,21d,22d] In diffusion experiments on nanoporous materials, Geier et al. have shown that using τ_s=16.0 and τ_b =1.6 for the tortuosities in zeolite crystals produces a model that more closely agrees with experiment.[23d] This implies that the surface is playing a larger role in the total diffusivity than was previously expected. Culbertson et al. measured the diffusion coefficients of several dyes in microfluidic channels with a depth of 10 to 15 μm and a width of 30 to 46 μm using a static imaging method and three dynamic methods—stopped flow, varying the applied potential (E-field

method), and varying the detection length (length method). The reported values deviate from each other and from literature values by as much as 11%. Experimental error is cited as the cause of these deviations, but it could be that surface effects were skewing the measurements.

There are several hypotheses that suggest that the deviations from theoretical predictions in these experiments are the result of the drastic increase in the surface area to fluid mass ratio.[19d,20d,21d,22d] At large critical dimensions, surface effects can be neglected when modeling a fluidic system because most of the interaction occurs in the bulk of the fluid. Consider for example a pipe that carries fluid to a kitchen faucet. Most of the water molecules in the pipe interact with other water molecules of the fluid. Only a few molecules will make contact with the pipe, and in the case of laminar flow, those molecules will be relatively stationary because of the no-slip boundary condition inherent in this flow regime. The small-scale topology and morphology of the surface will have little influence on the bulk flow of fluid in a large pipe. If the diameter of this pipe is reduced, however, more interactions will occur at the inner surface of the pipe, and the effect of surface anomalies will become magnified. If the diameter of the pipe is reduced to the diameter of a water molecule, the predominant mode of interaction is between water molecules and pipe molecules rendering the classical fluid flow models completely useless. Thus, the influence of the surface on flow characteristics and hence the efficacy of the classical models scales inversely with the characteristic dimension of the channel. [19d,20d,21d,22d] Ultimately all forces either in the bulk or at the surface are electro-magnetic in nature [20d] and bulk forces, although stronger, are dissipated in three dimensions while surface forces are dissipated in only two. At some length scale, the

magnitude of these forces will intersect. It has been shown empirically in biological studies that at a length scale of less than 1mm, surface forces begin to dominate over the bulk body forces.[19d,20d,21d,22d]

It is clear that continuous fluid flow models need to be modified to account for the anomalies inherent in microscale flow regimes. As the length scale of devices continue to decrease down into the nanoscale, however, it will not be adequate to think of and model a liquid as a continuous object. At the nanoscale, models will have to consider molecular interactions instead.[19d,20d,21d,22d] The Knudsen number is a quantity used to determine how small is too small for the continuum models previously described. The Knudsen number is the ratio of the distance between fluid molecules and the hydrodynamic diameter of the device. For $Kn \le .001$, the fluid can be thought of as continuous and the continuum models can be used. For larger values, $.001 \le Kn \le 0.1$, the fluid must be thought of as a system of particles, and the continuum model must be altered to account for things such as slip at the boundary. For $0.1 \le Kn$, the continuum model must be abandoned all together. The Knudsen number is defined by

(49)

$$Kn = \frac{\lambda}{\delta},$$

where λ is the mean free path between gas molecule interactions and δ is the hydrodynamic diameter of the channel. For liquids, following Probstein, the lattice spacing defined by

(50)

$$\lambda \approx \left(\frac{V}{Na}\right)^{\frac{1}{3}},$$

where V is the molar volume of the fluid and Na is Avogadro's number, is used instead of the mean free path. For water, λ is 0.3 nm, and this means that for channels narrower than 300 nm, more sophisticated models than the ones described above must be used.[21d,22d,24d] This estimate assumes smooth cylindrical channels and may be too narrow an estimate.

4.10 Knudsen Tortuosity

As was stated earlier, Geier et al. [23d] have found that the self- component of diffusion is greater than the bulk- component. This result has been predicted theoretically for pores that are *fractally* rough. Froment, Coppens, and Malek [25d,26d,27d] have shown that the self-component of diffusion is strongly affected by the fractal dimension of the surface.

Coppens and Fromment have shown that the self-diffusion of a porous material is given by

(51)

$$D'_K = D_{oK}\left(\delta'\right)^{ds-2}$$

where δ' is the ratio of the radius of a particle to the maximum *fjord* size on the surface of the membrane, and *ds* is the *fractal adsorption dimension* of the pore surface. The *fractal adsorption dimension* is a measure of the roughness, over all length scales, of the surface of a pore. A completely rough surface would be fully 3-dimensional (*ds*=3) while a perfectly smooth surface would be 2-dimensional (*ds*=2). Comparing Equations 51 and 8a implies that

(52)

$$\tau s = \left(\delta'\right)^{2-ds}.$$

The reasoning behind this equation is that smaller particles have access to more surface area on a rough surface than larger particles. This will lead to more interactions with the surface, and thus slow the rate of self-diffusion. Monte Carlo simulations have confirmed the predictions made by this model. [25d,26d,27d]

Figure 4.13 shows a log plot of the total diffusion when the roughness of the surface is taken into account. Here *df* is used to approximate *ds*. As can be seen, the diffusivity of very small particles is attenuated due to interaction with the rough surface. In the previous part, the component of self- diffusion was neglected since the average pore size was found to be approximately 1 μm. This made the self-diffusion negligible compared to the bulk diffusion when the self- and bulk-tortuosities are equal. Figure 4.13 implies that the surface cannot be ignored, even when the hydrodynamic diameter of the pores is greater than the 300 nm, because the self and bulk tortuosities are not equal. It should be noted that Malek and Coppens have a more sophisticated model for the diffusive scaling factor that includes a function describing the probability of a particle

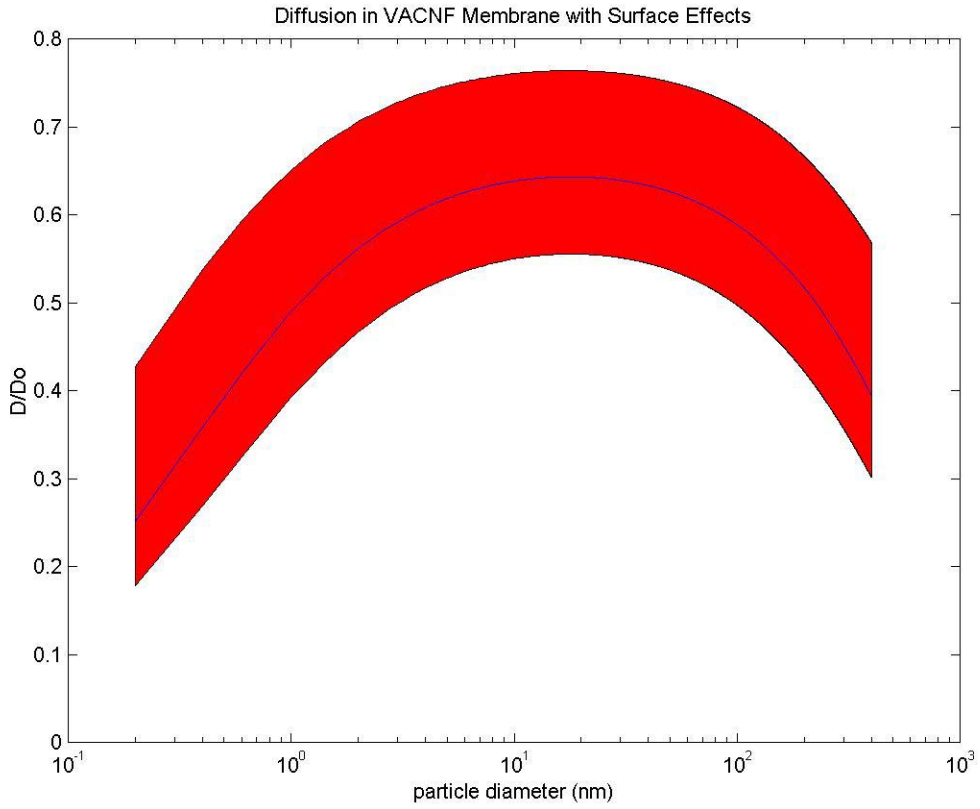

Figure 4.13 Surface Calibrated Normalized Diffusion Constant versus Particle Diameter. The lower boundary represents diffusion at the base of the fibers while the upper boundary represents diffusion at the tips. The blue line is the average. This plot was generated by using df for Ds in equation 52.

becoming stuck in a fjord, or recess on the surface.[25d,26d,27d] This could lower the total diffusion even more, suggesting that self diffusion cannot be neglected even in relatively large pores or channels. Certainly surface phenomenon such as adsorption, stearic forces, and Van Der Waals forces will scale the self-diffusivity.[20d,21d] These physical phenomena may be accurately modeled by assigning an effective fractal-adsorption-dimension to the surface.

In this part, a modern approach was used to determine the hydrodynamic characteristics of VACNF membranes. The results of this part show a slight dependence of permeability on the disorder of the fibers. There is a somewhat strong dependence of diffusion on surface roughness. It is not clear at this time how surface roughness will affect permeability. In order to be a truly nanofluidic device, the surface has to play a large role in transport. It is here where interactions can be specifically tailored to produce devices with selectively permeable membranes. At this time, the pore size is too large to effectively mediate the transport of macromolecules.

Bibliography 4

[1d] Andrade, J. S., Street, D. A., Shibusa, Y., Havlin, S., and H. E. Stanley *Phys. Rev. E* **1997**, 55, 1.

[2d] Havlin, S., Ben-Avraham, D. *Advances in Physics*, **2002**, 51, 1, 187.

[3d] Perreau, M., Peiro, J. and Berthier, S., *Phys. Rev. E* **1996,** 54, 4590.

[4d] Sukop, M.C., G.J. van Dijk, E. Perfect, and W.K.P. van Loon, *Transport in Porous Media*, 48, 187.

[5d] B. B. Mandelbrot, 1982 *The Fractal Geometry of Nature,* Freeman, San Francisco.

[6d] Bunde A and Havlin S (ed) 1996 *Fractals and Disordered Systems* Berlin: Springer.

[7d] A Franz et al, *Nonlinearity*, **2001**, 14, 1411.

[8d] A Hunt G Gee, *Advances in Water Resources* **2002** 25, 129.

[9d] Ogston, A. G., *Faraday Soc. Trans.,* **1958,** 54, 1754.

[10d] Yu, B. M., Liu, W., *AIChE*, **2004,** 47, 50.

[11d] Katz, A. J., A. H. Thompson, *Phys. Rev. Lett.,* **1985** 54, 1325.

[12d] B. Yu & J. Li *Fractals*, Vol. 9, No. 3 **2001** 365.

[13d] Mandelbrot, B.B. 2002. *Gaussian Self-affinity and Fractals*, chap. IV. New York: Springer.

[14d] Given J A and Mandelbrot B B *J. Phys. B: At. Mol. Phys.* **1983** 16 L565

[15d] Guerrini, Swartzendruber, *Soil Science*, **1997**, 162(11), 778.

[16d] Reis, *J. Phys. A: Math. Gen.* 29 **1996,** 29, 7803.

[17d] Kim, M. H., Yoon, D. H., Kim, I. *J. Phys. A Math. Gen.* 26 **1993** 5655-5660.

[18d] Dasgupta, R., Ballabh, T. K., and Tarafdar, *S., J. Phys. A: Math. Gen*. 32, **1999,** 6503.

[19d] M Elwenspoek; T S J Lammerink; R Miyakei; J H J Ruitman; *J. Micromech. Microeng*, **1994** 4, 28a.

[20d] C Ho Y Tai, *Annu. Rev. Fluid Mech*. **1998**, 30, 579.

[21d] Mohamed Gad-el-Hak (ed), *The MEMS Handbook*, CRC Press, 2002.

[22d] Mohamed Gad-el-Hak, *J. Fluids Eng*., **1999**, 5, 121.

[23d] Geier, Vasenkov, and Kärger , *J. Chem. Phys*., **2002**, 117, 5.

[24d] Probstein, RF *Physicochemical Hydrodynamics: An Introduction, second edition*, John Wiley & Sons, New York, 1994.

[25d] M.-O. Coppens and G. F. Froment, *Fractals,* **1995** 3, 807.

[26d] K Malek and M Coppens, *Phys. Rev. Lett.,* **2001**, 87, 12.

[27d] K Malek and M Coppens, *J. Chem. Phys*., **2003**, 119, 5.

Appendix 4

```
%%This program examines a top down SEM image of a VACNF forest and
%%computes its hydrodynamic properties
%%Eric Hullander 2005 ORNL



map=colormap;
count=0;
phi=0;
truck=0;
duck=0;
fick=0;
s=(-1)^.5;
border=0;
rs=[1:2000]*1e-8;
a=(100*10e-6)
b=(100*50e-6)
delta=(2*a*b)/(a+b)
Lo=50e-4;
A=a*b
Rc=2*75/(A*delta^2)
ratio1=0;
Rm=0;

kappa=0;
```

```
d=0;
phi=0;
rf=0;
df=1.8
pix=50e-7
Db = [1.7810    1.8740    1.9150    1.9410    1.9610];
X = [50    75   100   125   150];
Df=polyval(polyfit(X,Db,5),50:150);
Da=Df;

file2='C:\Documents and Settings\Eric Hullander\Desktop\ORNL\Data\Membrane\Analysis\Figures\fibersSEM2.bmp';
[fick]=imread(file2,'bmp');
[x y]=size(fick)
Area=x*y

for thresh=50:150
  eps=thresh-49

  for i=1:x
    for j=1:y
      if fick(i,j)>thresh;
        duck(i,j)=1;
      else duck(i,j)=0;
      end
```

```
    end
  end

  %pic=num2str(eps)
  %filename=cat(2,'C:\Documents and Settings\Eric Hullander\Desktop\New
Folder\phi',pic,'.bmp')
  %imwrite(40*duck,map,filename,'bmp')



  a=zeros(x,1);
  b=zeros(1,y+1);
  duckx1=[b;a duck];
  duckx2=[b;duck a];
  ducky1=[a duck;b];


    deltaxyduck=abs(duckx2-ducky1);
    deltayduck=abs(duckx1-ducky1);
    deltaxduck=abs(duckx1-duckx2);
    border=deltaxduck+deltayduck+deltaxyduck;
  bordera=border/2;
  for i=2:x-1
    for j=2:y-1
      if border(i,j)==2&border(i,j-1)~=1&border(i,j+1)~=1&border(i-1,j-
1)~=1&border(i-1,j)~=1&border(i,j+1)~=1
        border(i-1,j)=1;
```

```
    border(i,j)=3*s;
    border(i+1,j)=1;
    border(i-1,j-1)=1;
    border(i,j-1)=1;
    border(i+1,j-1)=1;
    border(i-1,j+1)=1;
    border(i,j+1)=1;
    border(i+1,j+1)=1;
  end
  if border(i,j)==2&(border(i,j-1)==1|border(i,j+1)==1|border(i-1,j-1)==1|border(i-1,j)==1|border(i,j+1)==1)
    border(i-1,j)=1;
    border(i,j)=1;
    border(i+1,j)=1;
    border(i-1,j-1)=1;
    border(i,j-1)=1;
    border(i+1,j-1)=1;
    border(i-1,j+1)=1;
    border(i,j+1)=1;
    border(i+1,j+1)=1;
  end

  if border(i,j)==1&border(i+1,j)==2&border(i,j-1)~=3
    border(i-1,j)=1;
    border(i,j)=1;
```

```
            border(i+1,j)=1;
            border(i-1,j-1)=1;
            border(i,j-1)=1;
            border(i+1,j-1)=1;
            border(i-1,j+1)=1;
            border(i,j+1)=1;
            border(i+1,j+1)=1;
          end
        end
      end
      %store picture of fiber borders
      %pic=num2str(eps)
      %filename=cat(2,'C:\Documents and Settings\Eric Hullander\Desktop\New
Folder\border',pic,'.bmp')
      %imwrite(40*abs(border),map,filename,'bmp')



      %Calculate phi, volume fraction of fibers
      phi(eps)=sum(sum(double(duck)))/Area;
      B(eps)=(1-phi(eps))^(1/(Df(eps)-2));
      B(eps)
      M(eps)=(B(eps)^2*(1-phi(eps)));
      L(eps)=(B(eps)^2-M(eps))^.5;
      %fractal scaling exponent
```

```
A1(eps)=B(eps)/(B(eps)-L(eps));
A2(eps)=L(eps)/(B(eps)-L(eps));
A3(eps)=(B(eps)^2-L(eps)^2);
zeta(eps)=log((1/A2(eps))*log(A1(eps)+A2(eps)))/log(B(eps));
dwl(eps)=log(A1(eps)*A3(eps))/log(B(eps));
dwu(eps)=log(((1/A1(eps))+A2(eps))*A3(eps))/log(B(eps));

  %fiber count
count(eps)=imag(sum(sum(border)));
%Calculate fiber radius in cm
rf(eps)=((phi*pix^2*Area)/(count*pi))^.5;
spe(eps)=1-phi(eps);
%Calculate inter-fiber spacing
d(eps)=rf(eps)*(exp(log((.75/0.0572)*((1-phi(eps))/phi(eps)))/2.377));
%Calculate permeability
kappa(eps)=.0572*(rf(eps)^2)*(d(eps)/rf(eps))^2.377;
  %Calculate resistance of one plane
Rm(eps)=1/(kappa(eps)*A);
%Calculate relative resistance
dp(eps)=d(eps);

%calculate hydrodynamic pore diameter
lamda1(eps)=(2*(dp(eps))*10e-4)/(10e-4+dp(eps));
taus(eps,:)=(lamda1(eps)./rs).^(Da(eps)-1);
```

```
  taub(eps,:)=exp(phi(eps)^.5.*((rs+rf(eps))./rf(eps)));

  %Fractal permeability
  %unity tortuosity, corresponds to classical model
  DT(eps)=1;

  %mean hydrodynamic diameter of largest pore

  kappaf(eps)=(pi/128)*(Lo^-1/A)*(2/(3+DT(eps)-2))*lamda1(eps)^(3+DT(eps));
  %Ogsten tortuosity, using maximum lambda from 10 in Yu Li

  DT(eps)=(phi(eps)^0.5/(log(Lo/lamda1(eps))))+1;
  DT2(eps)=((log(.75)+phi(eps)^0.5)/(log(Lo/lamda1(eps))))+1;
  kappaf2(eps)=(pi/128)*(Lo^-(DT(eps))/A)*(Df(eps)/(3+DT(eps)-
Df(eps)))*lamda1(eps)^(3+DT(eps));
  kappaf3(eps)=(pi/128)*(Lo^-(DT2(eps))/A)*(Df(eps)/(3+DT2(eps)-
Df(eps)))*lamda1(eps)^(3+DT2(eps));
  %kappaf2(eps)
  %kappaf(eps)
  %kappa(eps)
end
dmean=mean(dp);
meanDs=mean(taus);
meanDb=mean(taub);
stdDs=std(taus);
```

```
stdDb=std(taub);



rDtot=(meanDs/dmean+meanDb/3e-8)*3e-8;
Dstdtot=(stdDs/dmean+stdDb/3e-8)*3e-8;




meanphi=mean(1-phi);
stdphi=std(1-phi);



meanrf=mean(rf);
stdrf=std(rf);

meandp=mean(dp);
stddp=std(dp);

meancount=mean(count/(x*y*(pix^2)));
stdcount=std(count/(x*y*(pix^2)));

%classical resistivity, each slice is 100th of total
RM=100/sum(1./Rm);
%fractal resistivity
```

```
RMf=100/sum(kappaf*A);

RMf2=100/sum(kappaf2*A);

meanRf=RMf/Rc

meanRf2=RMf2/Rc

meanR=RM/Rc


save fiber



%%This program maps a top down image of a VACNF membrane to a surface, and
rotates it by 30 degrees %%to be compared with an image of a VACNF membrane tilted
30 degrees from the azimuth.


file1='C:\Documents and Settings\Eric
Hullander\Desktop\ORNL\Data\Membrane\MEMI\MEMISEM\cnfandsu8 002.bmp';

[straight]=imread(file1,'bmp');


file2='C:\Documents and Settings\Eric
Hullander\Desktop\ORNL\Data\Membrane\MEMI\MEMISEM\cnfandsu8 002.bmp';

[scew]=imread(file2,'bmp');


Figure(1)

image(staight)

Figure(2)

image(scew)
```

Figure(3)

mesh(staight)

Figure(4)

mesh(scew)

5 MEMBRANE:

Microfluidic Electro-Mechanical Barriers Realized with Arrays of Nanoporous Electrodes

5.1 VACNF Membranes in Microfluidic Channels

Vertically aligned carbon nanofiber (VACNF) growth is a bottom-up self-assembling process bypassing the need to arduously nanopattern porous structures. It has been shown that the void space of arrays of VACNFs can effectively be used as a size selective membrane for sub-micron particles and bacterial cells in microfluidic channels.[1e, 2e] Thus far, these structures have been sealed with PDMS lids that can easily slip and delaminate, damaging the underlying structures. To improve the durability of the devices and to make the devices more manufacturable, different materials were selected for the lid and the channels than were used in previous devices. The materials that were chosen were inexpensive, robust, biologically compatible, and can be processed using standard microfabrication techniques. These materials enabled the VACNF membranes to be permanently enclosed inside the microfluidic channel. The architecture of the device is illustrated in Figure 5.1. The structure took the form of a simple cross of SU-8 channels straddled by two VACNF membranes. The lengths of the membranes were 0, 2, 5, 10, and 50 μm, and the width spanned the breadth of the channel. The channels were bonded to an SU-8™ lid supported on a Mylar™ film.[3e] Theoretical predictions suggest that particles larger than 500 nm are too large to pass through the membrane. Extremely small particles, 500 pm, may be too small to easily pass through the membrane and depends on geometry as well as chemistry. Theory also

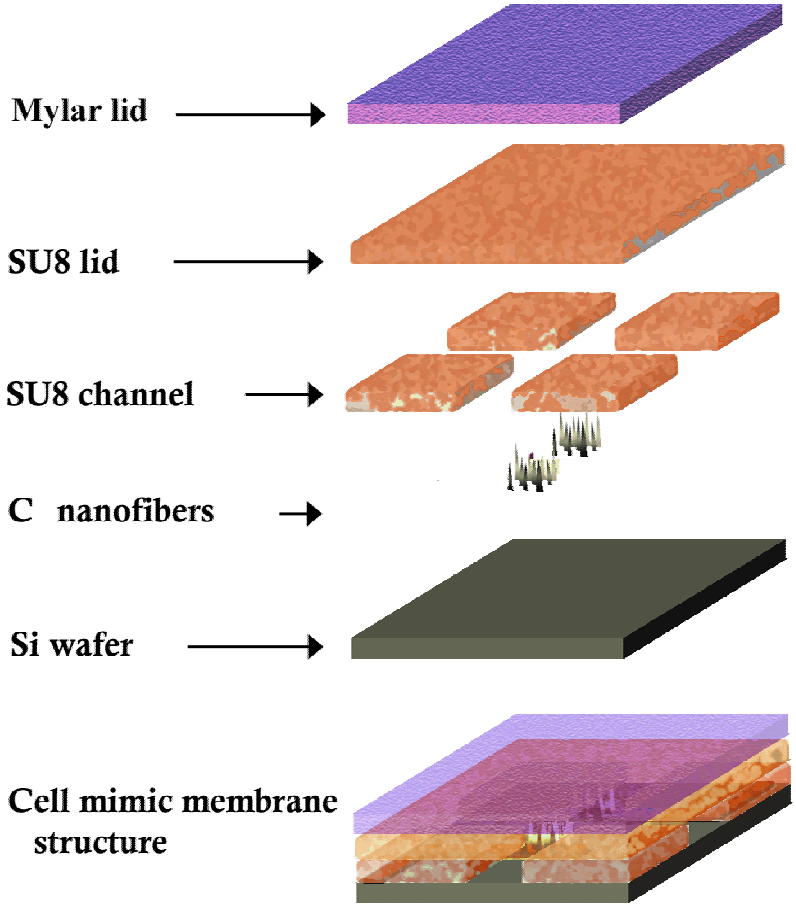

Figure 5.1 Construction of Membrane Mimic.

suggests that VACNF membranes offer little resistance to fluid flow. This is because they are disordered, and are mostly void space. The efficacy of the installed VACNF membranes was verified by showing that sufficiently large nanoparticles would remain trapped behind the barriers under pressure driven flows.[2e] Experiments were designed to measure the diffusivity and permeability of the membranes. These results were compared to theoretical predictions.

5.2 Fabrication

The process flow used to create the structures is illustrated in Table 5.1. Photolithography was used to pattern locations for VACNF growth. Shipley 1813 photoresist was spun on a 100-mm diameter silicon wafer at 4000 rpm for 1 min and baked at 115 °C for 1 min to drive off the solvent. The channels were exposed through a bright-field contact mask to define the membrane regions. The wafers were baked in an ammonia oven to reverse the image produced by photolithography, rendering the exposed areas glassy and less soluble than the unexposed areas. This is done to achieve a profile in the resist suitable for lift-off.[4e] Following the ammonia bake, the wafers were flood-exposed. This does not affect the glassy photoresist, but renders the areas previously unexposed soluble. These areas define the membranes. The wafers were developed in CD-26, removing the photoresist from the membrane region. A reactive-ion etch (RIE) was performed to “de-scum” the wafer in preparation for thin film deposition. The wafers were placed in an electron-beam evaporator where 100 Å of Ni were deposited over the entire surface. The sacrificial Ni was removed by dissolving

Table 5.1 Process Flow.

			
1. 4 inch Si Wafer	2. Spin 1813 4kRPM 1min, bake at 115°C 1 min	3. Exposure through membrane mask 4 sec	4. Develop CD-26 2 min, descum
			
5. E-beam evaporate 100Å Ni	6. Acetone Liftoff	7. PECVD of 12 µm VACNF	8. Spin 10 µm SU-8 2010
		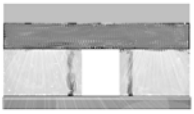	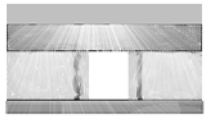
9. Bake at 70-90°C for 3 min, reflow at 150°C for 10 min	10. Expose through channel mask 8sec, PEB at 70-90°C 3 min, develop PGMEA 2 min	11. Seal with Mylar lid spin coated with 5 µm SU-8 2005	12. Expose, PEB at 70-90°C 3 min

away the glassy photoresist supporting it in acetone, leaving the Ni film only in the membrane-electrode regions. They were rinsed in isopropanol and dried with N_2 gas. VACNFs were grown from the Ni catalyst regions by way of PECVD. The fibers were grown to a height of 12 μm to facilitate sealing, and the recipe had to be adjusted to make the fibers strong enough to withstand subsequent fabrication steps. See Figure 5.2. Microfluidic channels were defined over the membranes. This was achieved by spinning 10 μm of SU-8 2010 at 4000 rpm for 1 minute. The wafer was soft-baked to drive off the solvent. Placing the wafer on a hotplate set to 70ºC and gradually raising the temperature to 90ºC in about 2 min achieved this. The wafer was held at this temperature for another minute to ensure the solvent was evaporated. Then, the temperature was gradually raised to 150ºC over the course of 10 minutes. This was to "reflow" the SU-8. The wafer was left on the hotplate while the temperature was gradually reduced back to room temperature. This was done to minimize thermal strain that had been causing the SU-8 film to delaminate. What remains of the bump after reflow can still be seen in Figure 5.3 and 5.4. The wafer was exposed through a photomask for 7-10 seconds to pattern the 10-μm deep, 50-μm wide channel structures onto the wafer. A post-exposure bake (PEB) was performed to finalize the cross-linking process. This was performed at 90ºC for 3 minutes. The wafers were developed for 2 minutes in PGMEA to create the microchannels, rinsed in isopropanol, and dried with N_2 gas. The structures were then observed under a SEM to insure all SU-8 was removed from the channels and fibers as shown in Figure 5.4. The lids were then prepared. In a technique adapted from Jackman et al. [3e], a 3x3" Mylar™ square was ultrasonically cleaned in acetone, rinsed in

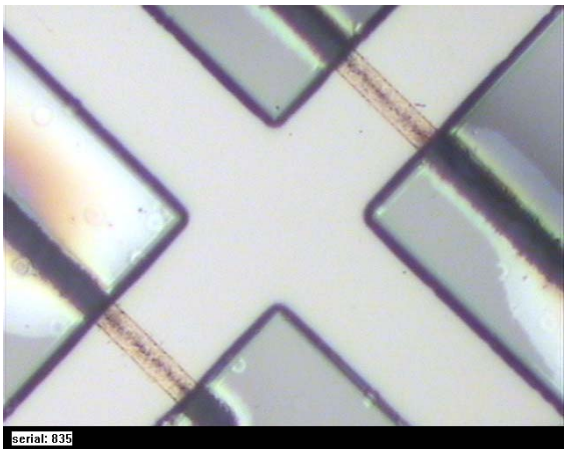

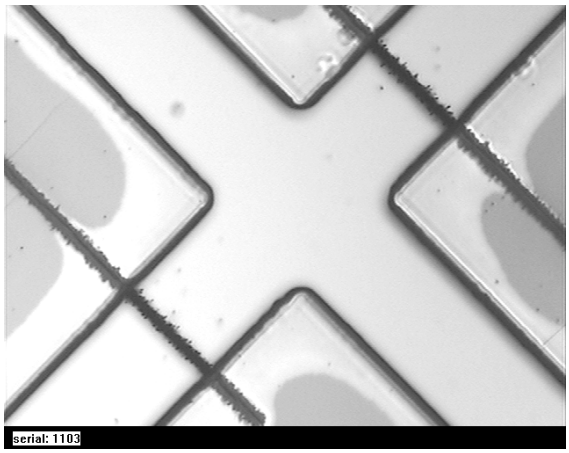

Fiber Failure Upon SU-8 development

Fiber after successful SU-8 development

Figure 5.2 Fiber Recipe Adjusted to Make Fibers Robust Enough to withstand Subsequent Microfabrication Process.

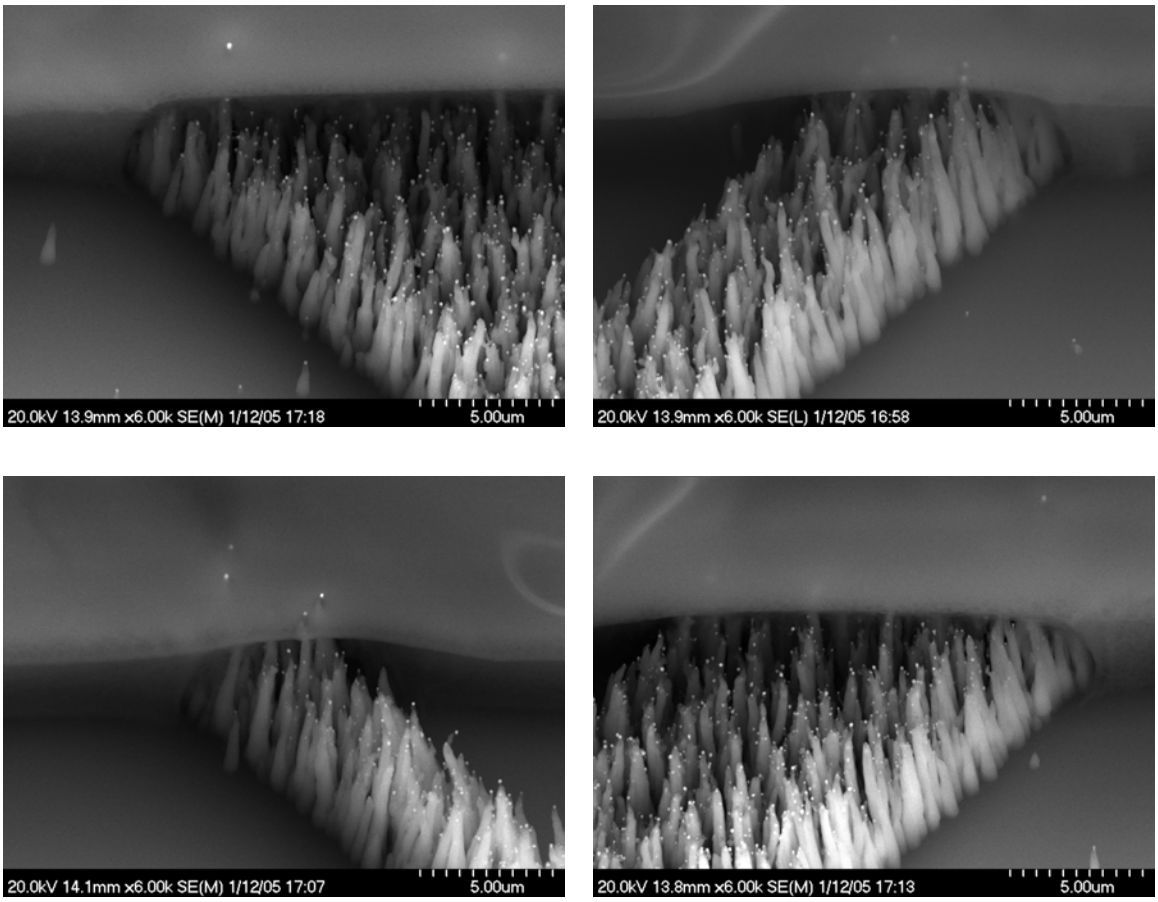

Figure 5.3 50, 10, 5, and 2 Micron VACNF Membranes at SU-8 Junction. Note the slight deformation in the SU-8 layer, and the match between the height of the fibers and the SU-8.

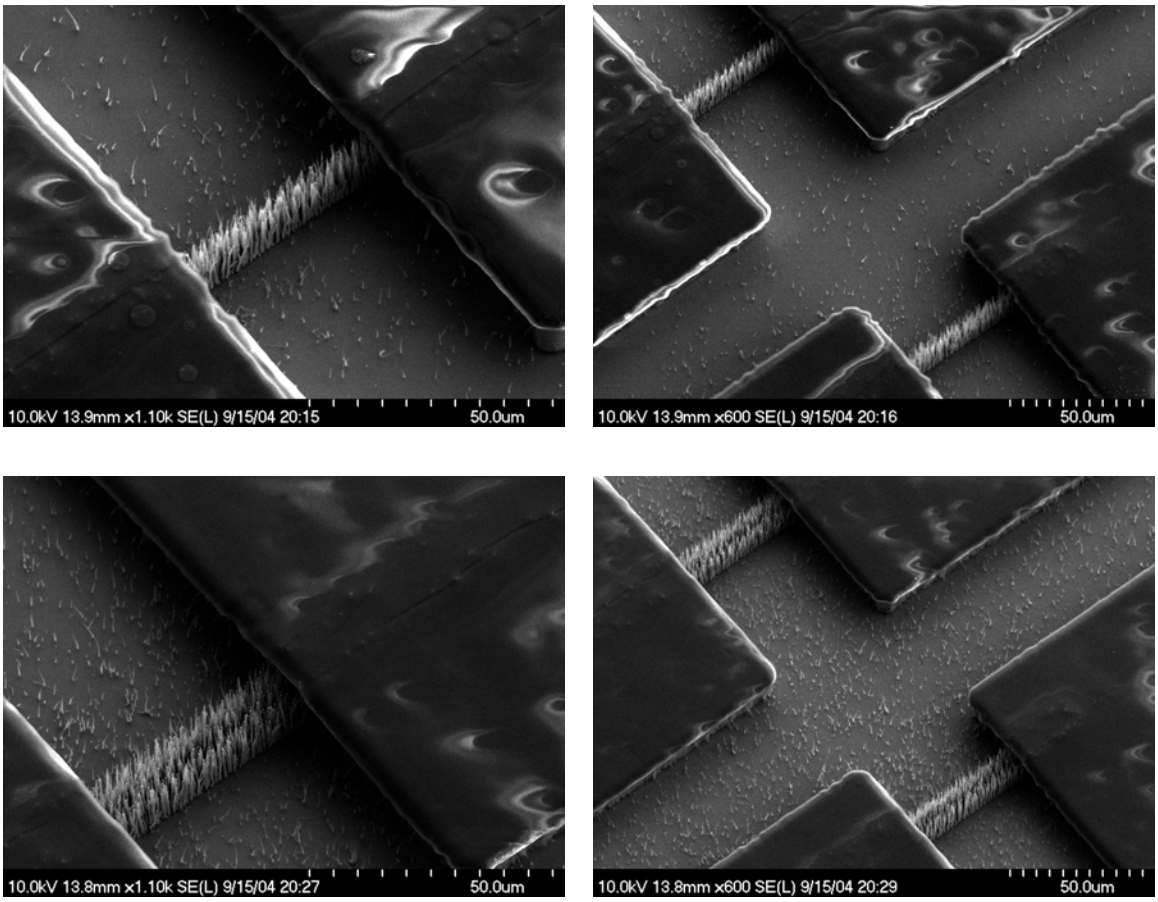

Figure 5.4 SEM of Unsealed Structures. Ni sputtering during fiber growth process caused extraneous fibers to grow in the channel. All SU-8 was removed from fibers.

isopropanol, and dried with N_2 gas. A 5-μm film of SU-8 2005 was spun onto the Mylar™ at 4000 rpm for one minute. The square was soft-baked to drive off the solvent. This was achieved by placing the wafer on a hotplate set to 70ºC and gradually raising the temperature to 90ºC over about 2 minutes. Next, 1/8" eyelets were punched in the Mylar™ to define the ports for fluidic access to the microchannels. This was done using a Precision-Brand™ punch and die kit. The Mylar™ lids were placed SU-8-side down onto the wafer, creating a sandwich of silicon, cross-linked SU-8, unpolymerized SU-8, and Mylar™. Light pressure was applied to the sandwich until much of the air gap was visibly removed. The wafer was flood exposed to crosslink the unpolymerized SU-8. The wafer was placed on the hotplate and post exposure baked from 70ºC to 90ºC to complete the crosslinking process, permanently bonding the structure together as shown in Figure 5.5. Incidentally, the fact that the crosslinking was effective proves that the structure is transparent to UV and suitable for fluorescence microscopy. Reservoirs, as shown in Figure 5.6, were placed over the eyelets so solution could be pipetted into the reservoirs until any static head pressure was neutralized. Vacuum could then be applied to the column of air above the liquid to pump fluids through the device. A manifold was constructed consisting of four pressure valves connected in parallel to each reservoir, and joined at the other end to the vacuum source. This allowed the pressure on each microchannel to be controlled externally without disturbing the device.

5.3 Fabrication Results

The biggest challenge in this process is ensuring that all mating surfaces are uniformly flat. This is necessary because small defects in the SU-8 layers can make

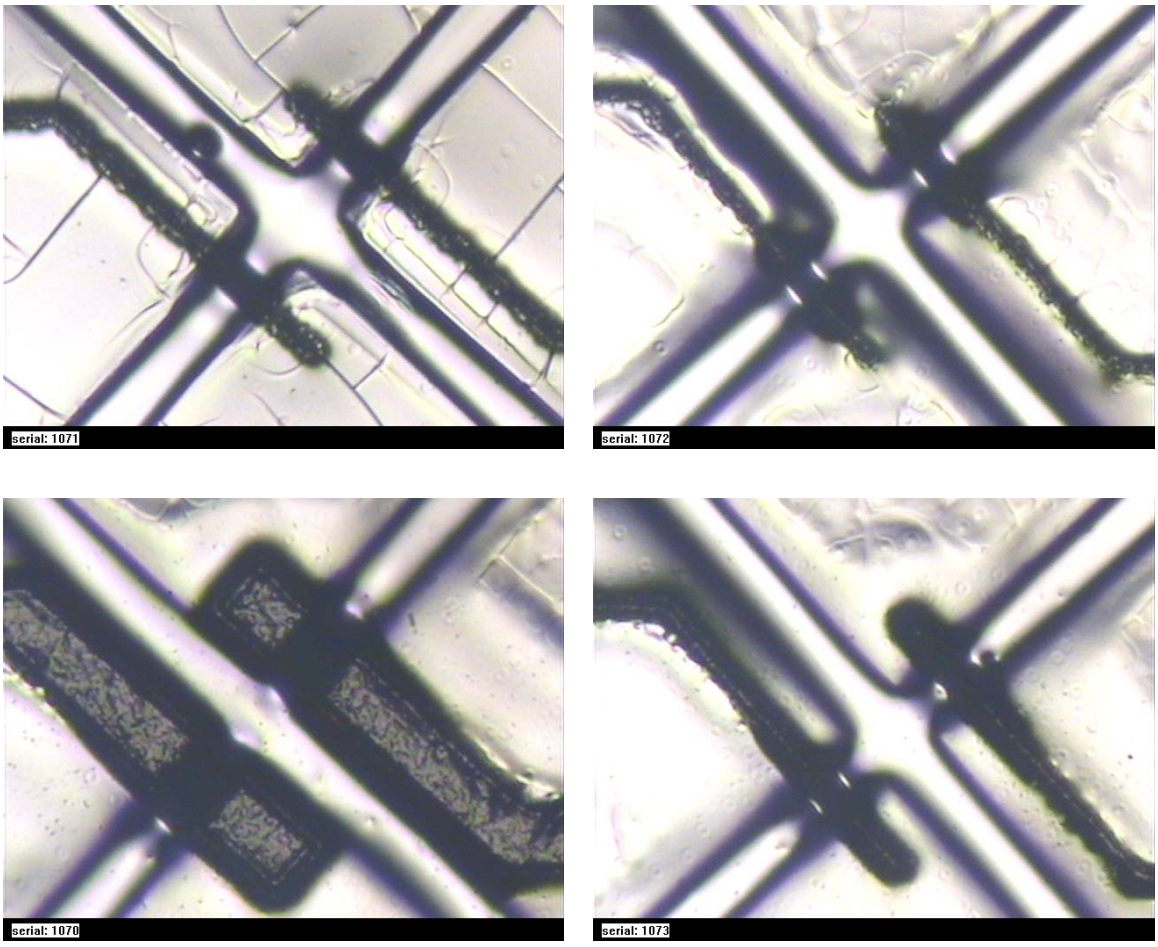

Figure 5.5 Sealed Microfluidic Structures. Note how SU-8 is forced into the channel near the fiber barrier.

Figure 5.6 Final Realization of the Device.

sealing the structure impossible while keeping the underlying channels and membranes intact as shown in Figure 5.7 Several methods were developed to minimize surface defects and hence improve the seal of the structures. First, shorter fibers were grown than in previous structures. Previously, the fibers were grown twice as high as the channels they were in to make sure the membranes mated with the PDMS ceiling of the structure. This was not necessary for the SU-8 ceiling. A good mating was achieved with 12-micron fibers in 10-micron channels. To further minimize defects in the SU-8 film, the SU-8 was re-flowed by baking at a higher temperature. After the SU-8 film was spun over the fibers, it was baked at a high enough temperature to reduce its viscosity and produce a more uniform surface. The temperature of 150°C was chosen because at higher temperatures, the SU-8 polymerizes, making it impossible to develop. It is necessary to gradually raise the baking temperature to prevent large bubbles from forming and to ensure that the top surface does not harden before the bottom surface, trapping solvent. These bubbles can be seen in Figure 5.8, and represent the latest baking procedure. If the bubbles are sufficiently small and scarce, they will not interfere with the conduction of fluid in the channel. In order to get fluid from outside reservoirs into the microfluidic structures, holes had to be placed in the lid. These holes caused defects in the SU-8 coated Mylar lid that compromised sealing. After several methods were tried such as pinning, drilling, and cutting, it was found that a punch-and-dye kit creates a hole with very few surface defects. In order to seal the SU-8 coated Mylar lid to the structure, care had to be taken to choose an appropriate sealing temperature and pressure. After several trials, it was found that for the best results, the applied pressure should be as light

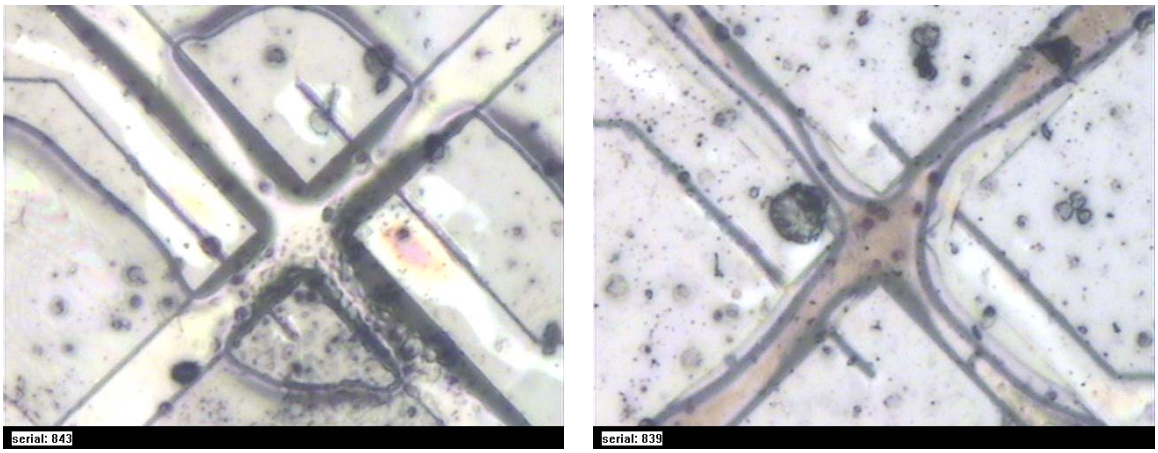

Too Cold Too Hot

Figure 5.7 Surface Defects Made Sealing Difficult. Controlling the sealing temperature helped alleviate these problems.

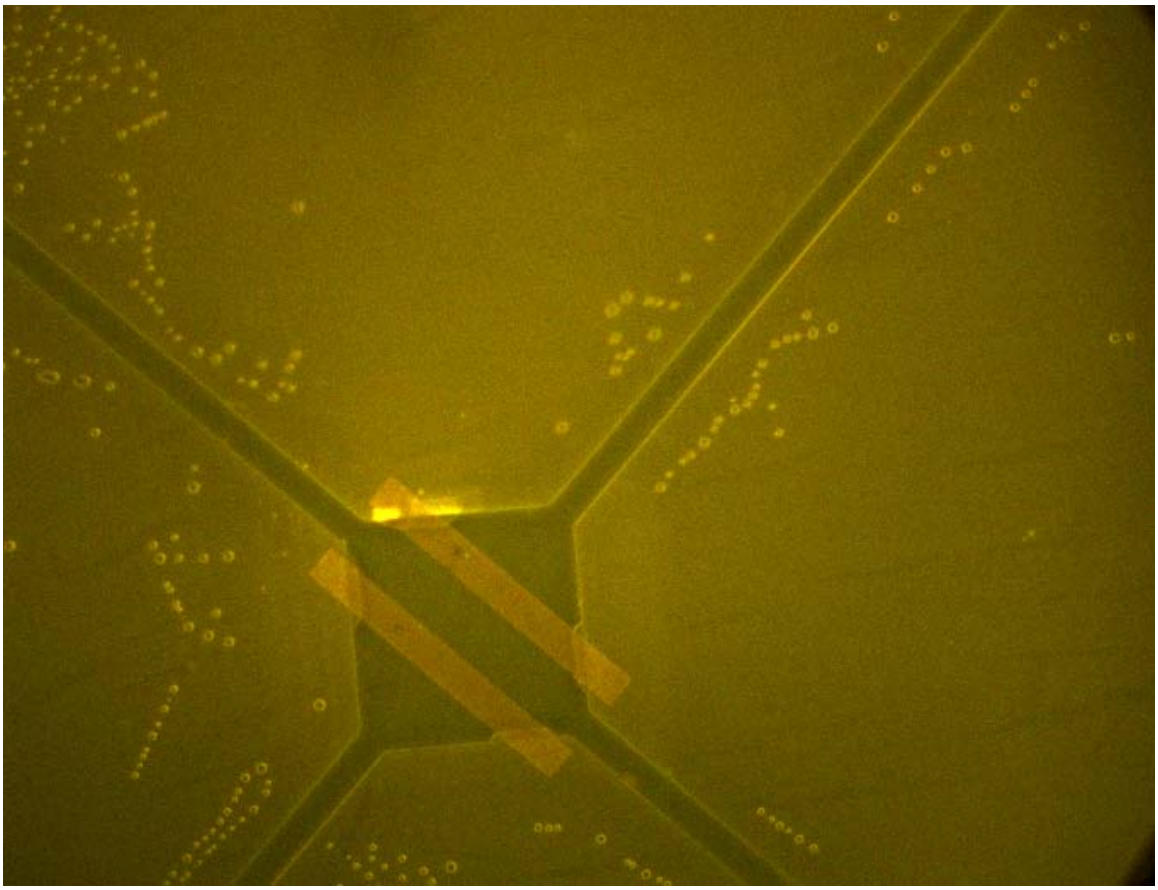

Figure 5.8 Final Structure.

as possible, and the sealing temperature should be at 70ºC. This temperature was chosen because it is warm enough for the un-polymerized SU-8 to soften, forming a conformal seal, yet cool enough to prevent the deformation of the underlying microstructures. After all of these precautions were taken, it was observed that a minute amount of SU-8 still deforms during the sealing process, and was enough to significantly compromise fluid flow through the channels. This deformation occurs just above the fibers and can be seen in Figures 5.8. At all of the places where the channel wall intersects the fiber membrane, a constriction of the channel can be seen which is caused by the SU-8 squeezing into the channel. In some instances the channel was completely closed, making diffusion and flow measurements impossible and otherwise rendering the device useless. To solve this problem, a new set of masks were produced that removed all extraneous fibers. Also, the span of the membranes at the intersection of the channels was widened to accommodate any pinching that might still occur. These new structures can be seen in Figures 5.8, 5.9, 5.10, and 5.11. Upon sealing, it was found that the 2 and 5 micron barriers had trouble supporting the ceiling across the wider gap. This is shown in Figure 5.12. This was not a problem for the 10 and 50 micron barriers.

5.4 Testing

To test these devices, the efficacy of the membrane again had to be verified. As before, fluorescently labeled latex beads were introduced into the microfluidic channels. To start, the bead size was chosen to be 750 nm in diameter. Pressure was applied to these channels causing the beads to engage the membrane. This can be seen in Figure 5.13. Once the efficacy of the membranes was verified, their fluidic properties could be

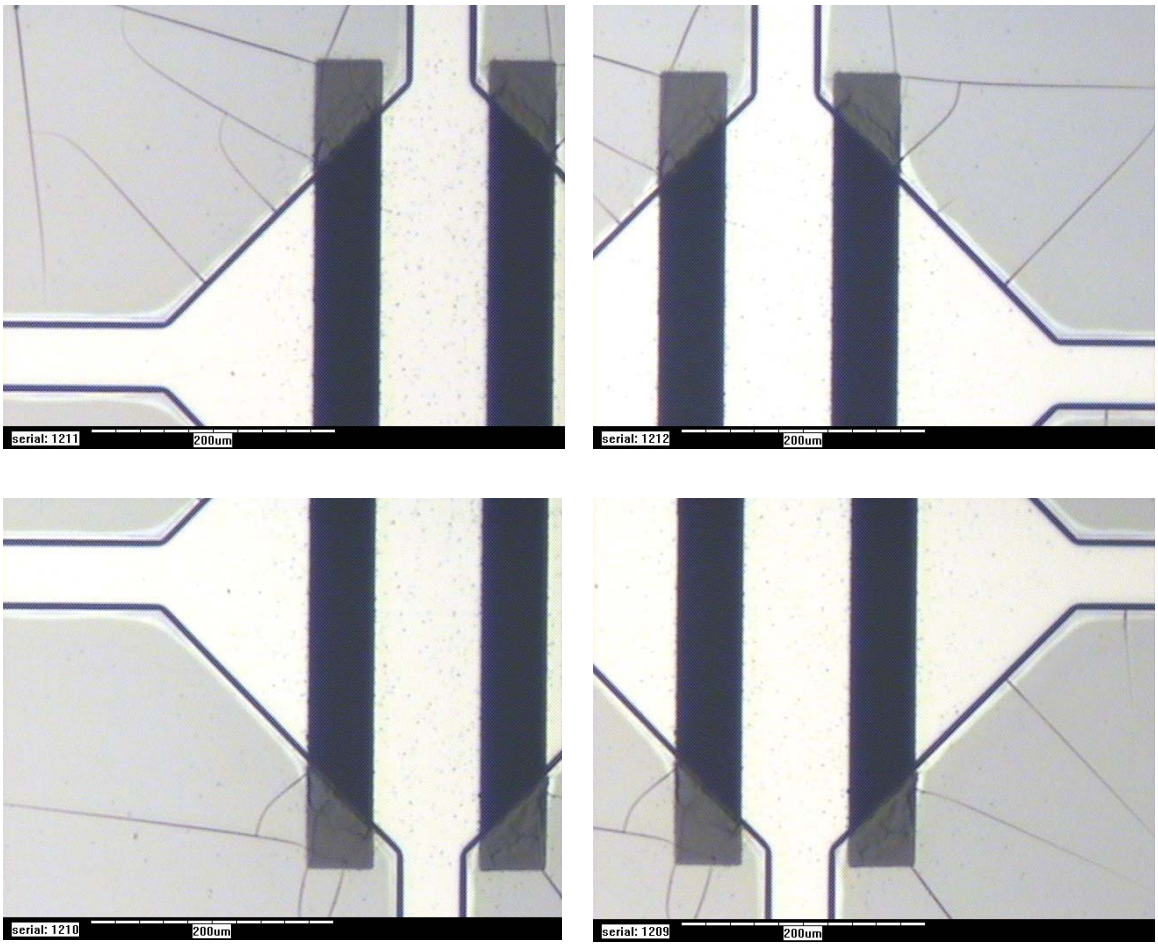

Figure 5.9 Composite of Unsealed Revised Membrane Structure. More clearance allows for SU-8 deformation during sealing.

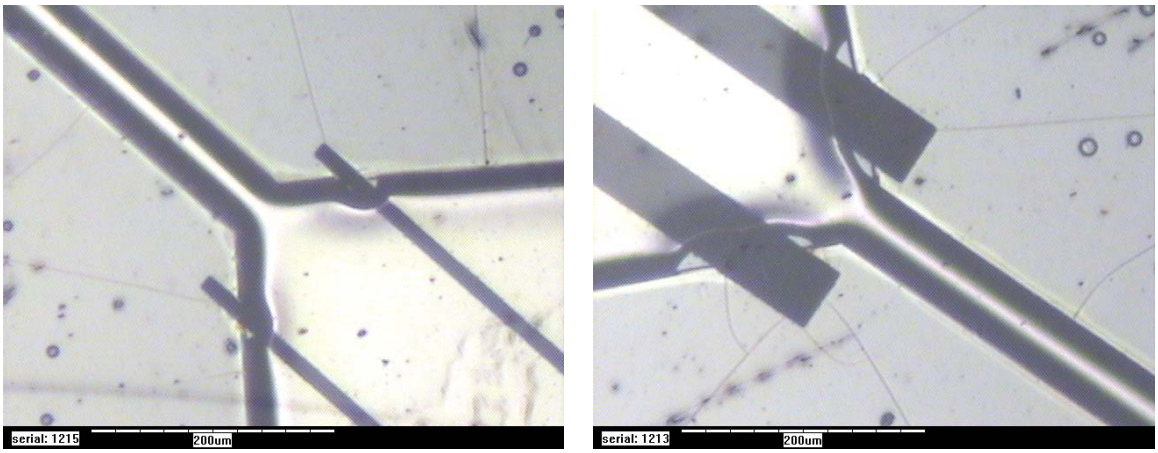

Figure 5.10 Composite of Sealed Revised Membrane Structure. SU-8 deforms into channel during sealing, but extra clearance allows for unrestricted flow through the membrane.

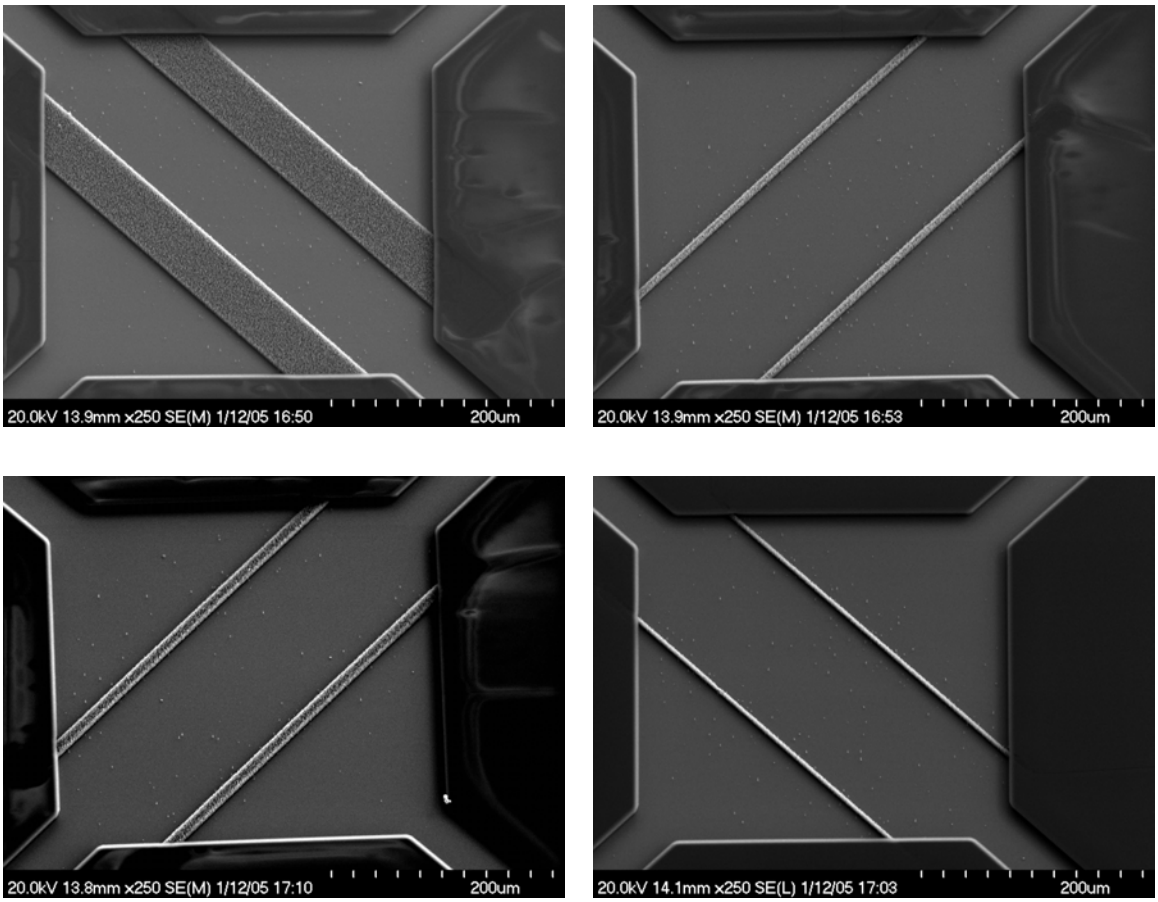

Figure 5.11 50, 10, 5, and 2 micron VACNF Membranes in Revised SU-8 Microfluidic Channels.

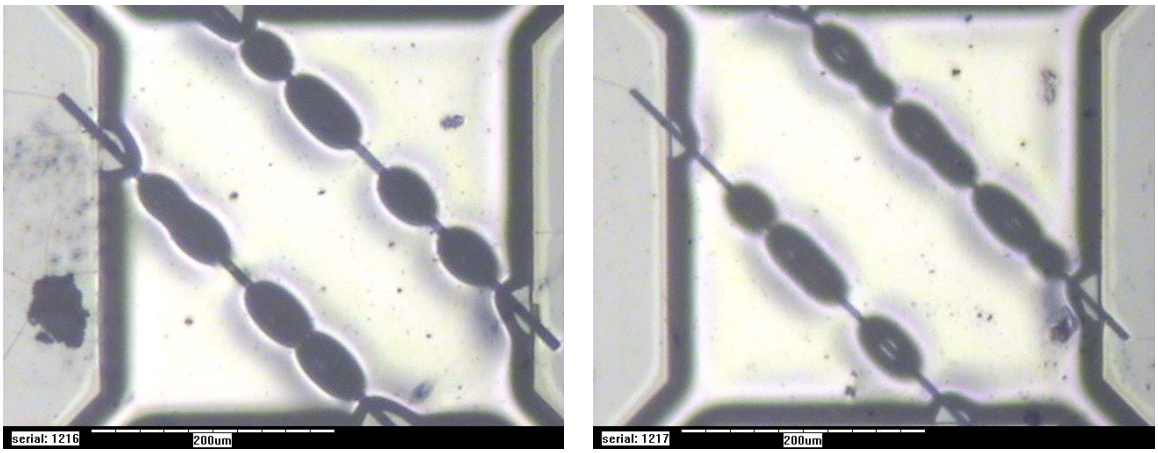

Figure 5.12 Ceiling Can Collapse with Wider Span in Revised Structures for Thinner Membranes.

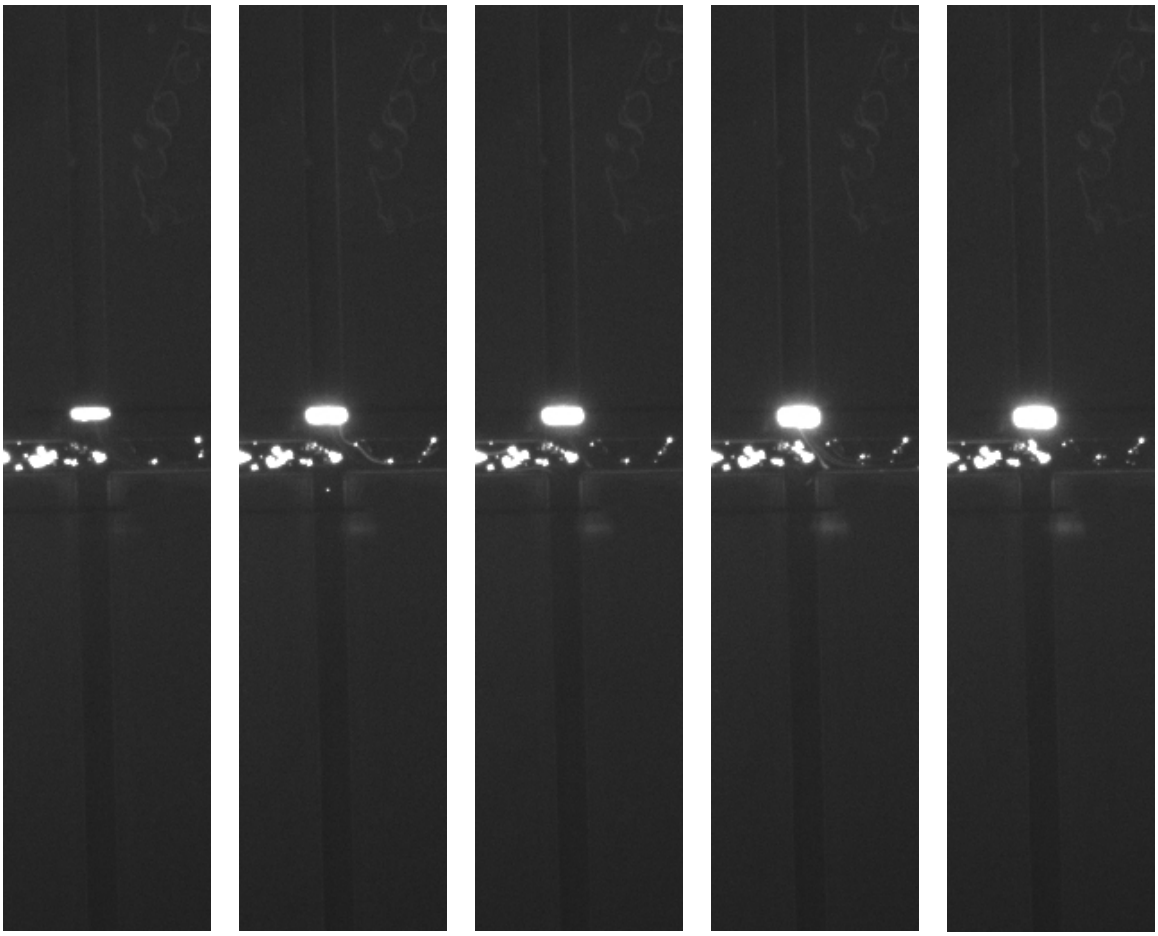

Figure 5.13 Time Series Beads and Membrane. 750 nm beads pulled against upper membrane cannot pass through. Beads tend to stick to extraneous fibers in channel and to membrane.

explored.

To develop the testing procedures and analytical tools necessary for the subsequent diffusion and permeation studies, the zero-length barrier structures as shown in Figure 5.14 were used as a control group. Diffusion constants were measured on these structures and compared to literature values. The efficacy of the procedures and tools was determined by their success at producing diffusion constants from experimental data that closely matched the literary values. A stopped-flow technique[5e] was used to find the diffusion coefficient, *D*. Fluorescein was pulled through one of the channels in the device that we will call the *x-axis* channel. Flow was stopped and images were captured once every second as the fluorescein diffused into the two side channels along the y-axis as shown in Figure 5.15.

Software was developed that analyzed this series of images. See Appendix 4 for a listing of this code. First, the software corrects for photobleaching, then proceeds to calculate the diffusion coefficient. Photobleaching is a phenomenon that occurs when a fluorophore in a fluorescent dye upon being exposed to a high intensity UV source loses the ability to participate in the absorption/emission process. The rate of photobleaching depends on the intensity of the light source. Significant photobleaching can occur in milliseconds even with sparse illumination. Recovery from photobleaching has been observed to be negligible, so the bleaching process is mostly permanent.[6e] Photobleaching cannot be ignored in diffusion measurements because it can cause large errors in the calculation of the diffusion coefficient, *D*. *N(x,t),* the brightness, should only be caused by diffusion according to Fick's Law. If it were a function of photobleaching

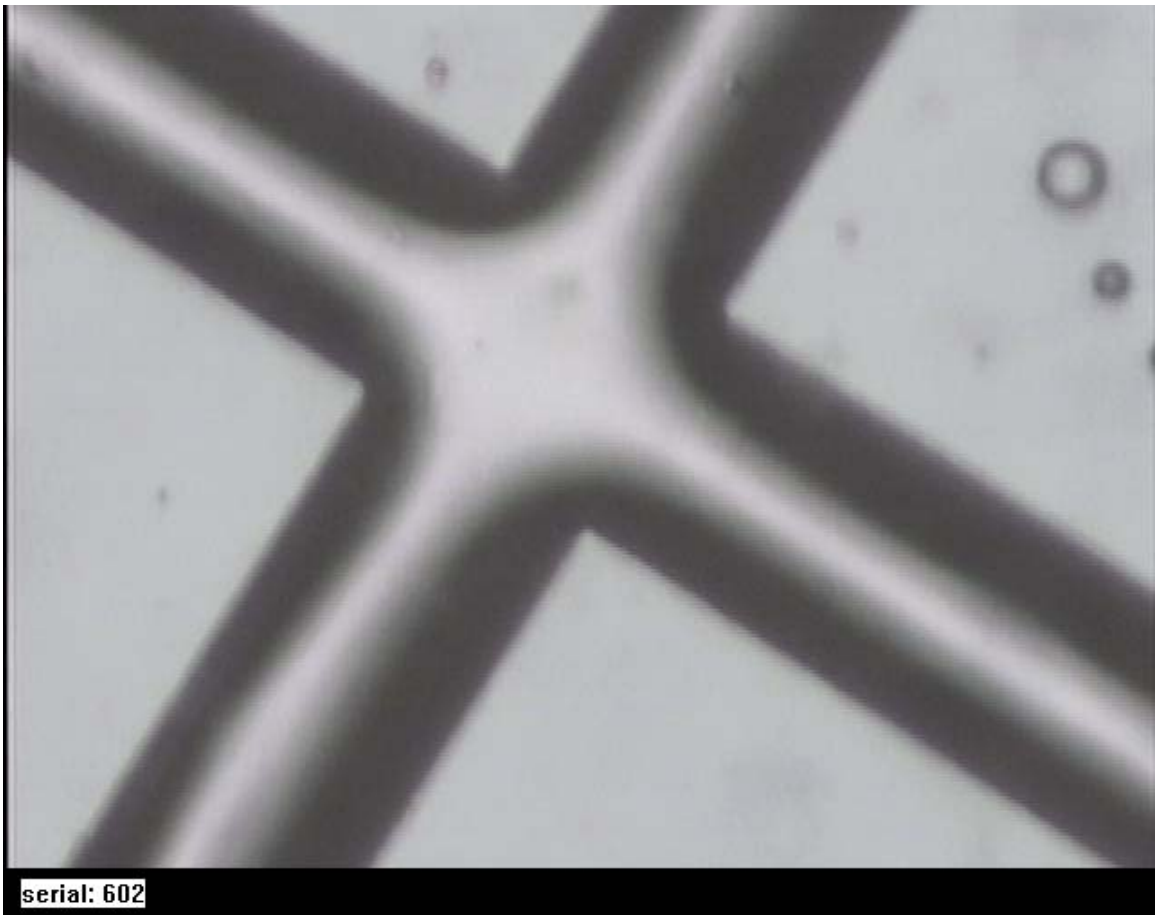

Figure 5.14 Sealed Fiberless Microfluidic Channel

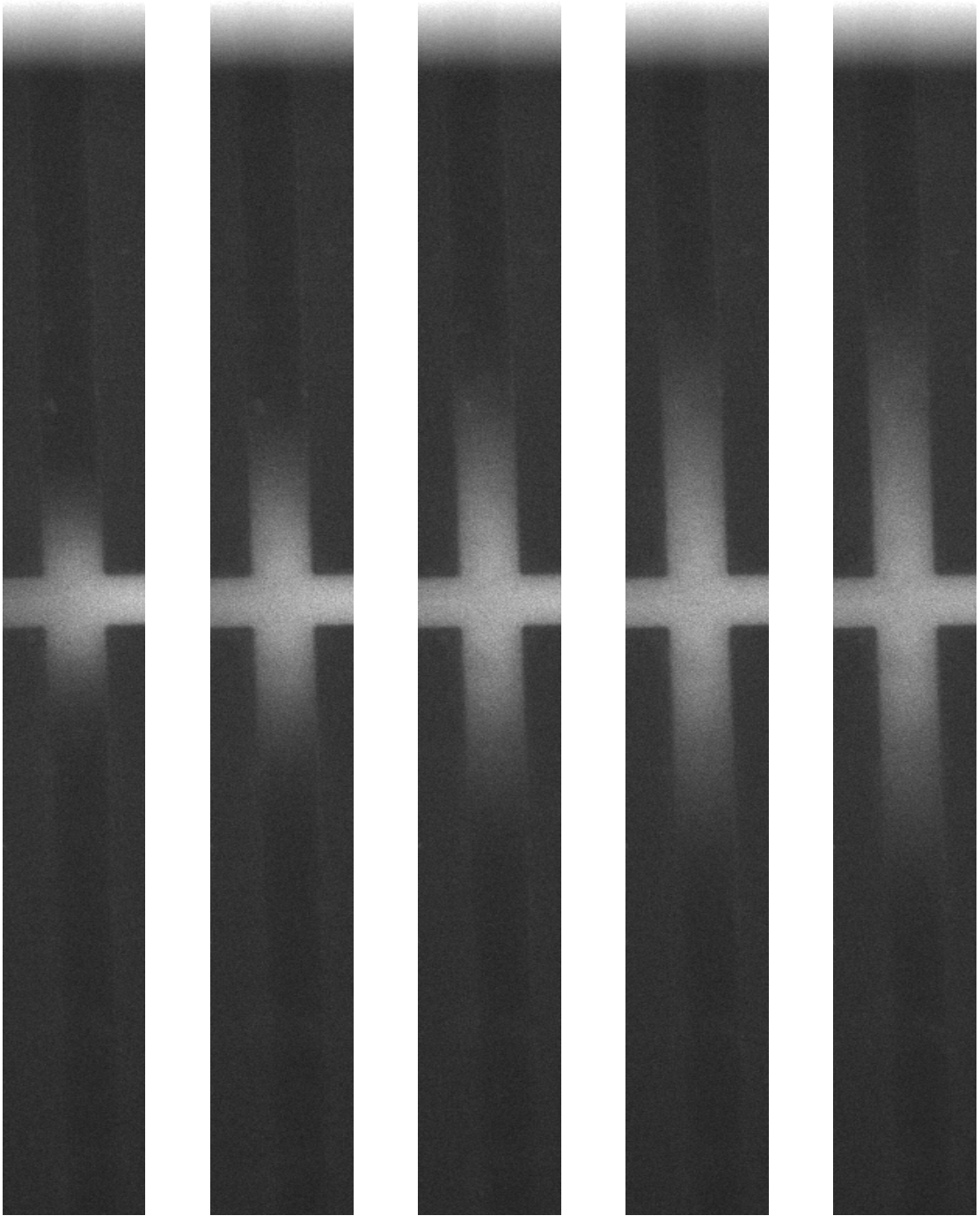

0 sec 5 sec 10 sec 15 sec 20 sec

Figure 5.15 Diffusion of Fluorescein. A solution of fluorescein diffuses into the upper and lower arms of the structure. The solvent was an aqueous isopropanol solution.

also, Fick's Law becomes

$$\frac{\partial N(x,t)}{\partial t} = D \cdot p(t) \cdot \frac{\partial^2 N(x,t)}{\partial x^2},$$

where *p(t)* is a photobleaching function. Substituting this back into Fick's Law and solving for the diffusion coefficient gives

$$D_\varepsilon = D + \frac{\partial p(t)}{\partial t} \cdot p(t) \cdot N(x,t),$$

where D_ε is the diffusion coefficient, D, plus some error. To correct for this, the photobleaching function was calculated and the diffusion data was calibrated accordingly. To find the photobleaching function, fluorescein was pumped into all of the channels, flow was stopped, and images were taken once every second as shown in Figure 5.16. Summing the total brightness of each image and fitting these to an exponential as a function of time gave the photobleaching function

$$p(t) = p_0 e^{-.0157t}.$$

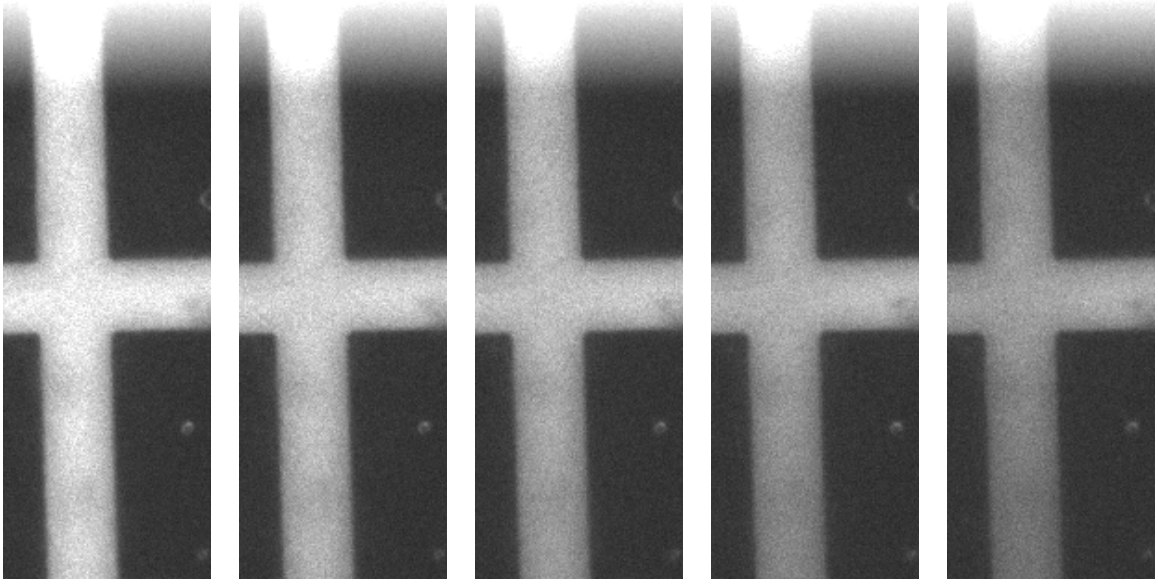

0 sec 5 sec 10 sec 15 sec 20 sec

Figure 5.16 Photobleaching. An image was sampled of every 5 seconds of the channels filled with fluorescein.

This was done with software code found in Appendix 4 and a plot of this data is shown in Figure 5.17. This function was used to calibrate the data collected for the diffusion experiments.

The software assumes that brightness is proportional to the density of fluorescein. Due to symmetry, the brightness in the *x-axis* was summed forming a *y* vector containing the total brightness in the *x* direction at every point along the *y-axis*. This operation was performed on every image in the series. All of the *y* vectors were concatenated into a matrix whose a_{mn} element was the brightness, and hence, density at a point m on the *y-axis* at a point *n* in time. Fick's second law of diffusion was used to solve for the diffusion coefficient, *D*.

Once the test procedure and software had been verified for diffusion on the control group structures, the test group (fibered structures) could now be characterized. The same stopped-flow technique used on the control was applied to the test structures as shown in Figure 5.18. The data was then analyzed using the same software as was used on the control group.

In order to determine the permeability of the membrane structures, fluorescein was pulled between the fiber barriers, while water was pulled through the membrane barriers as shown in Figure 5.19. The width of the band of fluorescein could then be used to determine the permeability of the membranes. For instance, if the membranes were shut off, then the fluorescein band would completely fill the channel. If the membranes were removed completely, the band would have some finite width. By comparing the

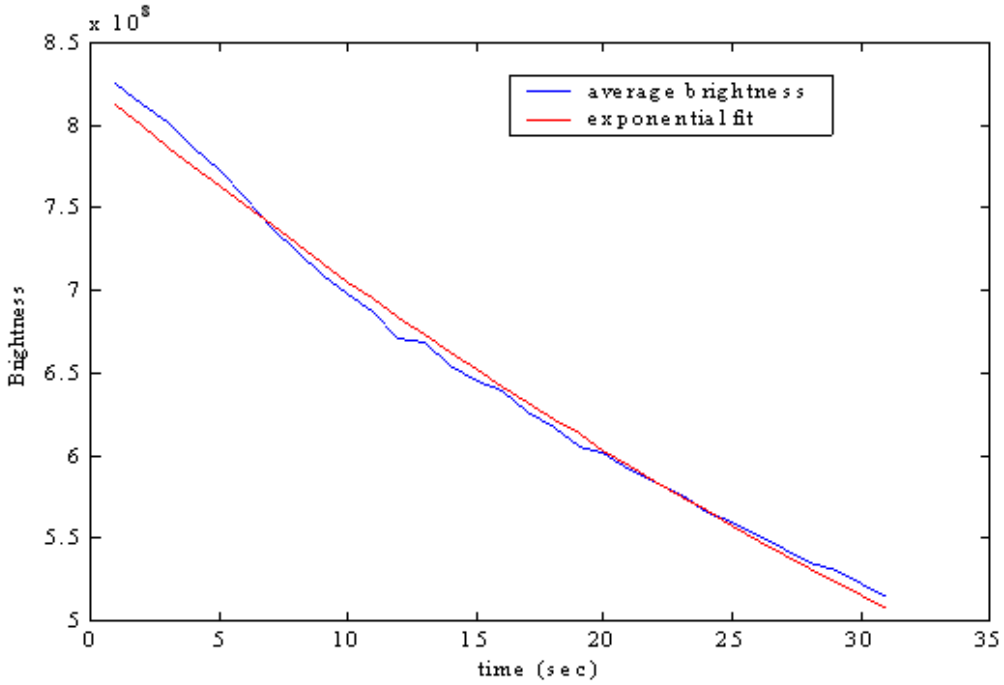

Figure 5.17 Plot of Brightness v. Time. Data collected from the images in Figure 5.16 to characterize the rate of photobleaching.

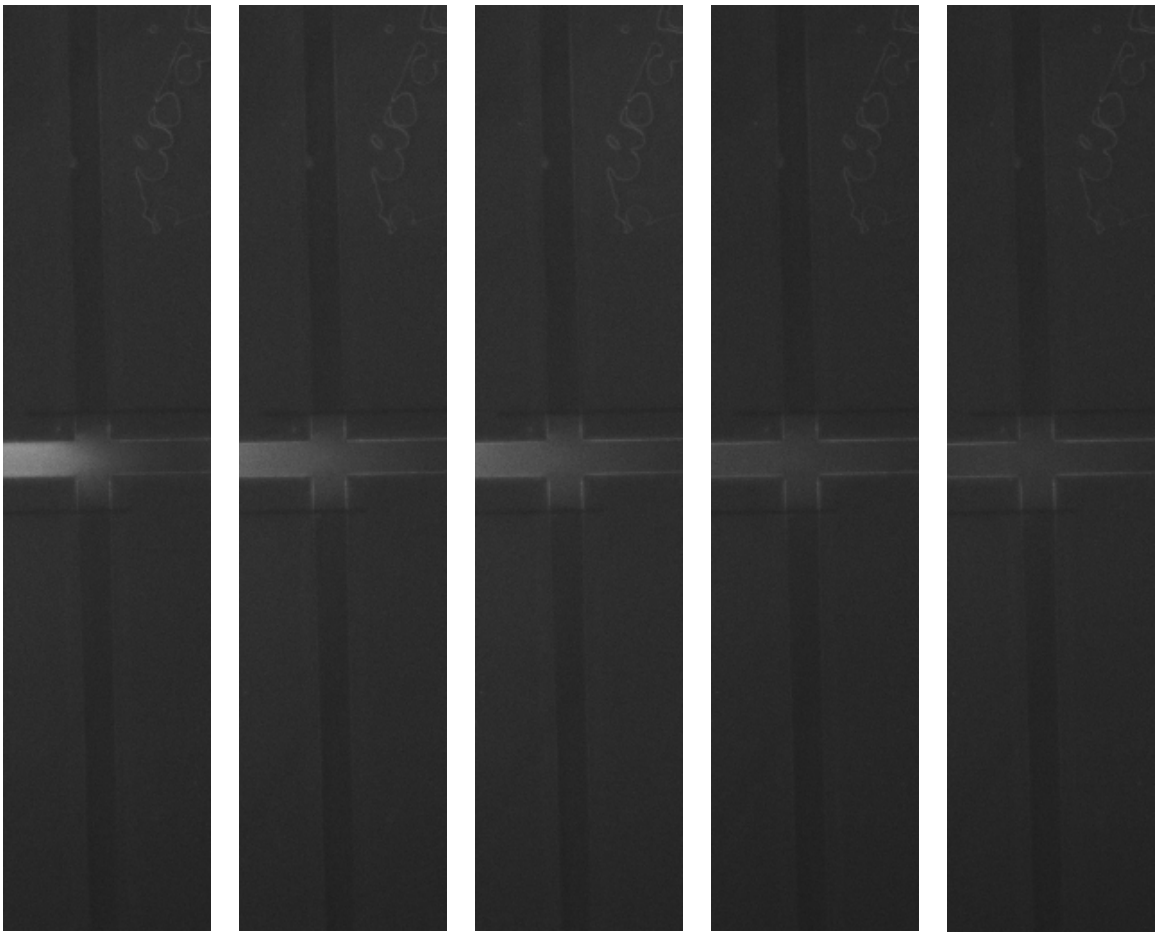

Figure 5.18 Time Series Fluorescein and Membrane. Fluorescein was pumped through the structure from left to right. Flow was stopped and diffusion was observed. Note the fluorescein does not cross the membrane barrier, implying the surface is playing a large role in the attenuation of diffusion.

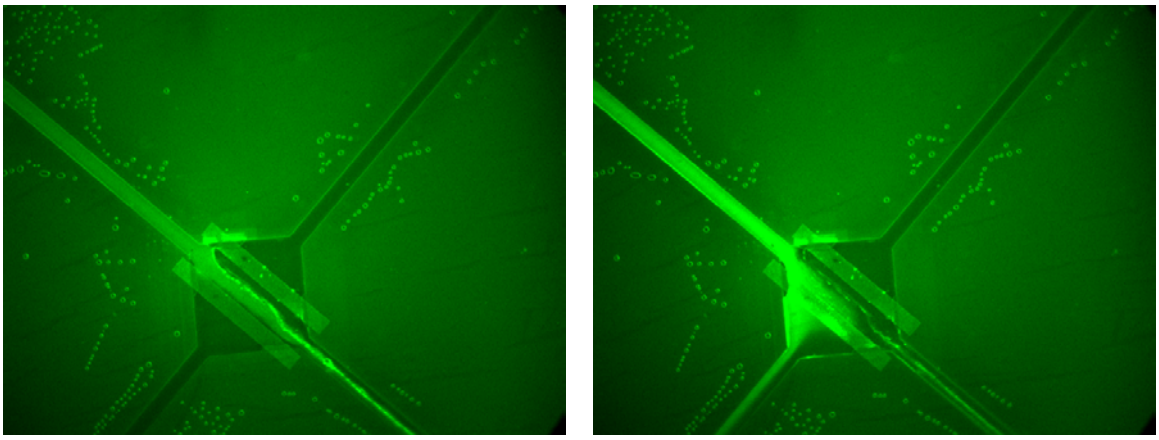

Figure 5.19 Fluorescein Flowing through Revised Membrane Structure.

width of the fluorescein band in unfibered structures to the width of the fluorescein band in fibered structures, one can estimate the relative permeability. Previously it was found that the flow resistivity of the membrane structures is only 50% greater than the channels they are in. This would mean that there should be no difference in the thickness of the fluorescein bands in the control and test groups.

5.5 Test Results

As can be seen in Figures 5.13 and 5.20 the membrane structure effectively stops beads larger than 750 nm from passing. Interestingly, when the beads found holes in the membrane which they could pass through, they quickly become clogged with the beads. It was also found that the beads themselves accumulated against the fiber barrier to form a semi-crystalline lattice. This is a process known as colloidal crystal formation.[7e] Colloidal crystals are self-assembling structures with a regular lattice spacing. Unlike the random distribution of nanofibers used as a membrane, the spacing between the beads is a precise function of the bead size and lattice structure. This could prove to be a precise method for controlling the pore size. The adsorbed beads proved to be robust and could not be easily removed. Also, the interbead spacing is both smaller than the interfiber spacing and smaller than the diameter of the bead, effectively reducing the pore size. To show this, 500 nm beads were flowed into the barrier of 750 nm beads, as in Figure 5.21, and indeed they too were trapped, forming yet another membrane with a pore size smaller still as shown in Figure 5.22. This process could be repeated to achieve pore sizes on the order of a few nanometers, closely approximating the size of a biological cell membrane.

With the membranes verified, the diffusion and permeation studies were

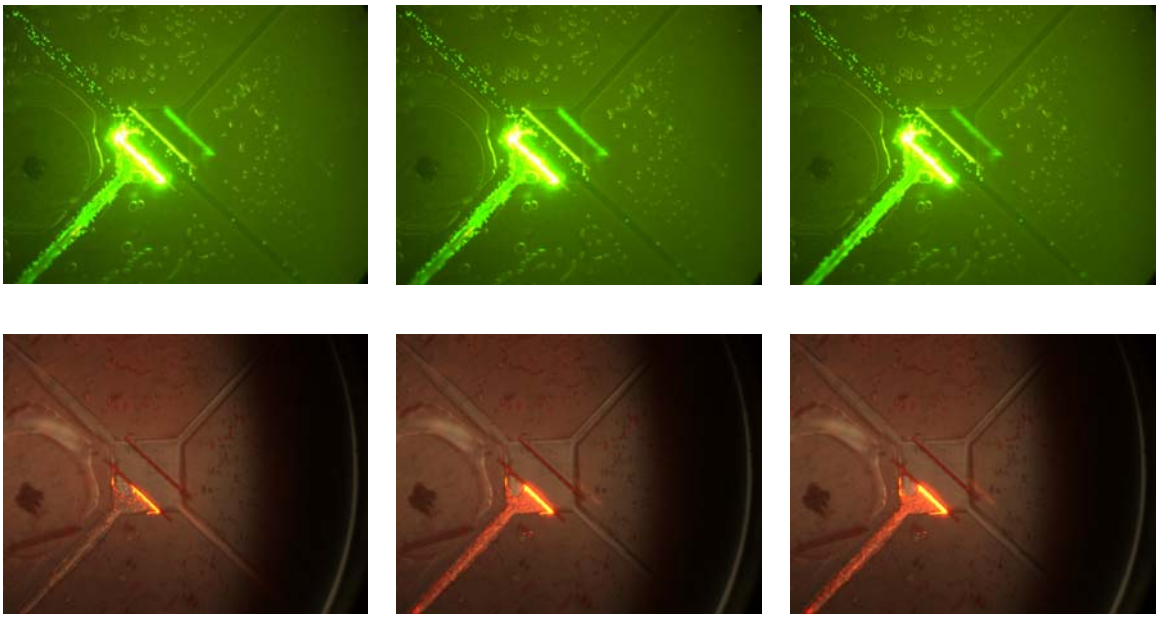

Figure 5.20 Time Series Colloidal Cake Membrane Formation on Carbon Nanofiber Membranes. From left to right, the top row shows 750 nm latex beads accumulating against fiber membrane. At first, beads find a leak in the membrane, but it becomes plugged. The bottom row shows 500 nm beads accumulating against the colloidal 750 nm cake. This is an effective means of controlling pore size.

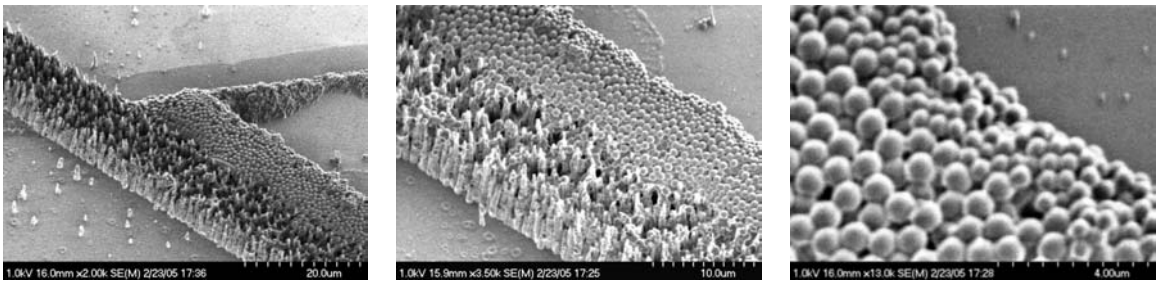

Figure 5.21 Structure in Figure 5.20 was Taken Apart and Imaged in an SEM to Show Colloidal Membrane Structure. Note the small variance in the reduced effective pore size.

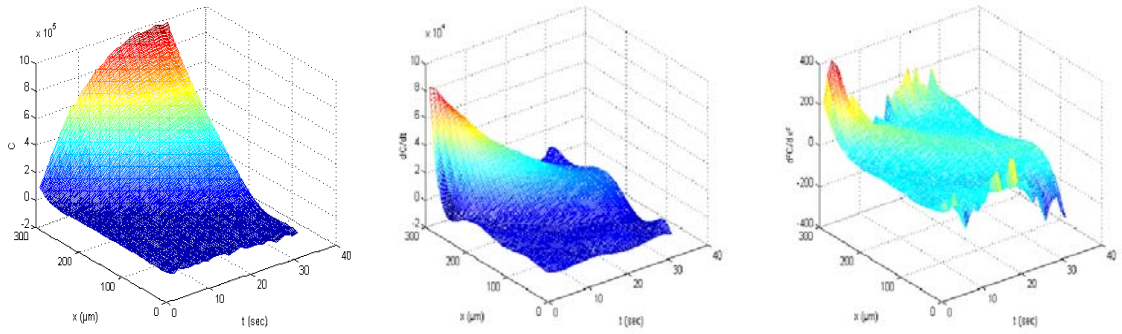

C(x,t) *dC(x,t)/dt* $d^2C(x,t)/dx^2$

Figure 5.22 Fluorescein Dynamics in Microfluidic Channel.

warranted. The diffusion constant, *D*, in the channels without fibers was found to be 2.2 ± 1.7 10-6 cm²s-1. Other sources report the value to be around 2.70 10-6 cm² s-1.[5e] The large uncertainty was due to having to sample a weak signal. The signal was weak because photobleaching would reduce the intensity from maximum saturation to total darkness in a time scale comparable to the diffusion process. The brightness of the lamp was reduced to its minimum value, and the gain on the camera was adjusted to its highest value to try to alleviate this problem. The program discriminated against points in the image that were outside of the active diffusing region. Sixty-six percent of the data was deemed useable. Plots from the output of this experiment are shown in Figure 5.23.

With the test apparatus and procedure working for the control group, diffusion measurements could now be made on the fibered structures. As can be seen in Figure 5.18, fluorescein did not diffuse through the membrane barrier, so it was impossible to calculate the membrane diffusivity this way. These results are inconclusive, but may be due to surface interactions between the fluorescein and the VACNFs. The experiment should be repeated with different dyes, and after treating the fibers with blocking solution.

The permeability of the membranes was found to be comparable to the permeability of the open channels. The thickness of the bands of fluorescein in both the fibered and unfibered structures was found to be about 15 microns, implying that the membranes offer little resistance to fluid flow.

Bibliography 5

[1e] B. Fletcher, E Hullander, A Melechko, T McKnight, K Klein, D Hensley, J Morrell,| M Simpson, M Doktycz, *Nanoletters*, **2004,** 4, 10.

[2e] L. Zhang, A. V. Melechko, V. I. Merkulov, M. A. Guillorn, and M. L. Simpson, *App Phys Lett*, **2002,** 81, 11.

[3e] R Jackman, T Floyd, R Ghodssi, M Schmidt, and K Jensen, *Micromech. Microeng*. **2001,** 11, 1–8.

[4e] MICROLITHOGRAPHY From Computer Aided Design (CAD) to Patterned Substrate, *Cornell Nanofabrication Facility* **2002.**

[5e] C. Culbertson, S. Jacobson, M. Ramsey, *Talanta* **2002,** 56, 365.

[6e] B. P. Mosier, J. I. Molho, and J. G. Santiago, *Experiments in Fluids* © Springer-Verlag **2002.**

[7e] O. Velev, A. Lenhoff, *Current Opinion in Colloid & Interface Science,* 5, **2000**.

6 Discussion

A microfluidic system was built to perform size selective separations on a nanometer scale. Membranes composed of vertically aligned carbon nanofibers performed these separations. In order to understand the physics of the device, several connections had to be made between existing models of transport through fibrous materials. In order to connect these ideas, several intuitive leaps had to be made and then verified. The first is that tortuosity, defined as a particle's path length divided by its displacement, is what scales the reference diffusion. The second is that the membrane can be thought of as a realization of some random fractal. The third is that tortuosity can be related to the resistance scaling factor, a property of a fractal. To support these claims, I show a close agreement between a classical and a fractal permeability model. The fourth is that I can incorporate a model to approximate surface effects, and this model can simply be added in parallel to the other models because it is an effect of tortuosity. This investigation shows that the surface cannot be categorically neglected because of the rather large device dimensions. The fifth is the extrapolation of 3-D information from an SEM image used to determine the parameters that fit into the models. Brightness was assumed to be a function of the vertical axis in 2-D grayscale images. The sixth is the unique use of materials in this project.

The device proved to be effective, although it is quite far from mimicking real cellular membranes. As of yet, the membranes are chemically passive, the pores are too large, and the membrane is too thick and permeable, although the membrane is self-assembling. The devices successfully filtered out fluorescently labeled particles greater than 500 nm in the passive diffusion case, and 750 nm in the presence of external

pressure. The device was constructed using standard microfabrication techniques and is biologically compatible. The best attribute of these devices is their flexibility. It is best to think of these devices as a modular platform or skeleton upon which technology will be built. Materials can easily be adsorbed to the fibers to control chemical and geometric properties. Further experiments should be carried out to measure the diffusivity and permeability of the membranes while tightly controlling all possible test parameters such as chemical composition and nanoscale device geometry. The influence of these parameters on permeation and diffusion is amplified at small scales. Regardless of whether or not the diffusivity and permeability of the devices can be precisely quantified, the devices can still be used as useful research tools. Though this device could have been realized by using other materials besides carbon nanofibers, carbon nanofibers offer great potential because of their chemical and electrical characteristics. We have already seen that latex beads readily adsorb to their surface. These beads could potentially be made chemically active to build a chemically selective membrane. It will also be interesting to investigate the electrical properties of the membrane. By applying an electric potential to the fibers by way of an electrode, ionic transport might be mediated. These investigations will be explored in the near future as this project continues.

Vita

Eric Hullander was born in Knoxville, TN on September 10, 1977. He graduated from Bearden High School in 1995 and entered the electrical engineering program at the University of Tennessee in 1996. He graduated in the spring of 2001 with a Bachelor's Degree of Science in Electrical Engineering. Following the completion of his Master's of Science, Eric plans to continue investigating the topics presented in this thesis.